Master's Thesis

Restrictions in the far-field of antennas enclosed in bodies of revolution

Clara Bäck

Department of Electrical and Information Technology,
Faculty of Engineering, LTH, Lund University, 2016.

Restrictions in the far-field of antennas enclosed in bodies of revolution

Clara Bäck
clara@jeca.se

RUAG Space AB
Solhusgatan 11, 412 76 Göteborg

Advisor: Daniel Sjöberg
Johan Wettergren

April 19, 2016

Printed in Sweden
E-huset, Lund, 2016

Acknowledgement

First and foremost, I would like to express my gratitude to my host company RUAG Space and my supervisor Johan Wettergren for giving me the possibility to gain insight to antenna applications for space industry. Without his tireless guidance, thoughtful advises and the encouragement, I would not have been able to get through the project.

I would like to express my sincere and deepest gratitude to my supervisor, Professor Daniel Sjöberg at the Faculty of Engineering, LTH, for his wise and valuable reflections when they were needed the most. His guidance has truly affected this master thesis.

A special acknowledgement goes to my family for their support during the good and bad days with the project as well as for helping me balance work and other aspects of my life.

Last but not least, I would like to thank the employees at the antenna group for making my stay at RUAG enjoyable. Thank you!

Lund, January 26, 2016
Clara Bäck

Abstract

Antennas can be found everywhere in our everyday life. One of the applications for them are space satellites, which can be used for communication, positioning and weather supervision. A satellite carries several components on its body, such as solar panels and cameras, therefore there is a volume restriction for the antenna to fit. This requirement gives rise to restrictions in the far-field for the radiation pattern.

The objective was to implement a calculation-tool by MATLAB, where theoretical surface currents on a structure could be calculated for a required far-field for a specified antenna outline. A genetic algorithm optimization generated feasible solutions and the MATLAB-tool evaluated the cost for it by comparing a far-field mask with the far-field given by the feasible solution.

The analysis was performed for two structures, a cylinder and a circular disc. Solutions were found when the dimensions of the structures were large, but the cost increased when the structures diminished. The solutions that were found were theoretical and not feasible in practice. A suggestion for excluding unphysical solutions is presented with a contribution to the cost function.

Key words:

Antenna pattern synthesis, body of revolution, far-field restrictions, genetic algorithm

Table of Contents

Chapter 1

Introduction

We have access to communication, position information and updated weather details wherever we go. We are connected all the time with our gadgets such as mobile phones, game consoles and activity bracelets, almost all of them are wireless one way or the other. Information is sent between the units with electromagnetic waves that are radiated from, or received by, antennas.

Electromagnetic waves are formed when an electric field couples with a perpendicular magnetic field. The fields propagate with the speed of light and are produced by the acceleration of electric charges. The science of electromagnetics was founded in 1873 by James Clerk Maxwell [1] and is best known by Maxwell's equations, which describe how electric and magnetic fields are generated and altered by each other and by charges and currents.

By varying the current in an aperture an electromagnetic wave arises. The aperture that radiates, or receives, electromagnetic waves is called an antenna. The first wireless communication was demonstrated by Heinrich Rudolph Hertz in 1886 and consisted of a $\lambda/2$ dipole with a wavelength λ of 4m [2, 3].

The modern antenna technology was not developed until World War II when new elements such as waveguides, horns and reflectors were developed [4]. In the second half of the 1900s, computer technology made it possible to analyse complex antenna systems in an accurate way. Today, commercial programs generate an initial design that can be manufactured as a working prototype. The challenge now is to design antennas within a certain volume and a specific radiation pattern. These requirements give rise to restrictions in the far-field.

In theory, any far-field can be generated from any volume without a volume restriction, a phenomenon known as "super directivity" [5]. In practice though, this is not realistic since this gives rise to currents that are substantially different for adjacent frequencies. Thus, there are limitations for the far-field for antennas that have a bandwidth.

One example of antennas with such limitations are space satellites, which can be used for communication, positioning, weather and geophysical supervision. These antennas face harsh space conditions and cannot be retrieved for maintenance or repair. Thus, the design needs to be reliable. Satellites must carry more than antennas on their body (i.e. solar panels and cameras), therefore there is a volume restriction for the antenna to fit. At the same time the footprint must be correct in order to cover the appropriate area [6].

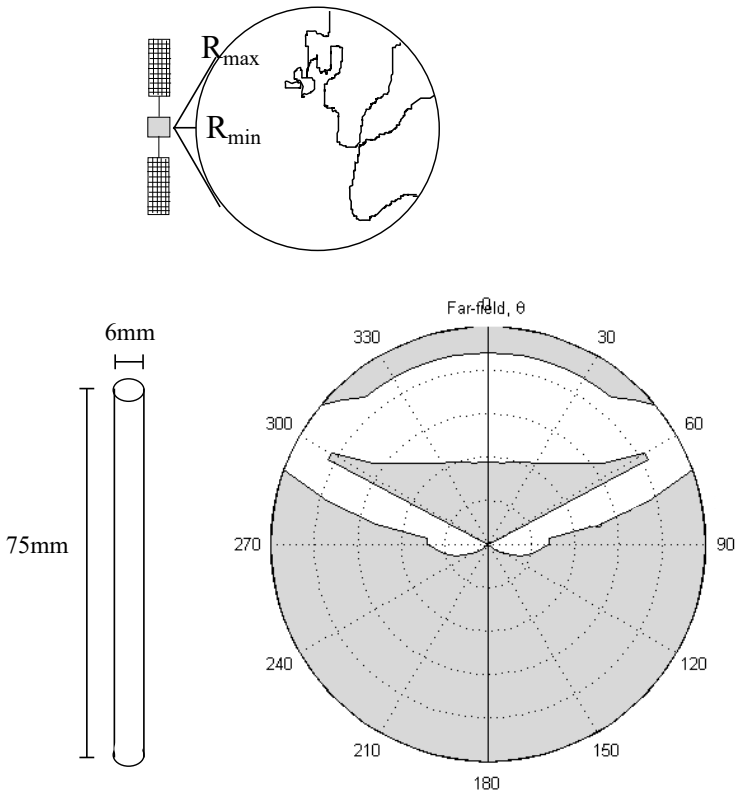

Figure 1.1: The desired footprint from a satellite antenna, the θ-angle in the polar plot is the angle from the cylinder axis. Is it possible to generate a far-field within the white area from an antenna within the cylindrical volume?

1.1 Background

Usually an antenna system is designed in order to yield specific radiation characteristics. This could be null in certain directions or a wide bandwidth. In this thesis the desired radiation pattern for an elongated cylinder shaped antenna is illustrated in Fig. 1.1. The satellite antenna covers the whole earth and has higher directivity in the outskirts on the covered area. The higher directivity will cover up for the longer distance to the poles.

The radiation characteristics for simple antennas such as dipoles, loops and helix antennas are known. More complex antenna systems that include several elements need antenna pattern synthesis, which is a method to design an antenna in order to obtain a certain radiation pattern [7]. There are different methods which can be used depending on the desired characteristics of the radiation pattern. Antenna pattern synthesis usually require two steps. First, a choice of an analytical model that represents the pattern approximately is needed. Secondly,

the analytical model needs to be matched to the physical antenna model [7, Ch.7].

Some common methods for three different categories of radiation characteristics are listed below. Schelkunoff polynomial method [8] is used for radiation patterns that prescribe nulls in specific directions. The required information for this method is the number of nulls and the location of them, the derived data are the number of elements for the array together with the coefficients. If the desired radiation pattern exhibits a specific distribution in the entire region a beam shaping method could be used, two of them are the Fourier transform method [9] and the Woodward-Lawson method [10] [11]. A third category of radiation characteristics are narrow beams with low side-lobes. Antennas with these characteristics could be handled by binomial methods [12] or Dolph-Tschebyscheff method [13].

Several commercial programs exist for calculations of the far-field for a given geometry and given sources. Why not just use one of these to solve the problem? In commercial programs both the structure and the boundary conditions are defined. In contrast, this case handles only the volume restriction, which makes the solution to the problem non-unique since only the amplitude of the far-field is defined and not the phase. By developing a code, the field solution does not need to be unique. On the other hand, several solutions can exist and the challenge is to find a solution that is physically feasible.

The antenna performance can be illustrated using the upper physical bounds for the directivity Q-factor quotient, D/Q. The directivity is the power density in the direction of the strongest emission compared with an ideal isotropic radiator with the same total power. The Q-factor, or quality factor, characterizes the resonator bandwidth relative to the resonator frequency and describes the damping of it. The upper bounds show the effect of changing the shape and size of the antenna geometry. Gustafsson et al [14] showed that optimal current distributions and upper bounds for D/Q can be determined for small antennas of arbitrary shape. "Small antennas" have a $ka < 1$ for the wavenumber k and radius a. The authors determined the analytical expression for D/Q by using the expressions for the current density and the stored energy. For small antennas the optimization problem was solved analytically and the closed form solution expressed the bounds in the polarizability of the antenna structure. For arbitrary size antennas the problem was solved numerically using Lagrange parameters in a method of moments formulation. A fairly large antenna with high directivity was used to generate physical bounds for the directivity Q-factor quotient. Inspired by Gustafsson et al [14], this thesis aims to find optimal currents on antennas for a predefined volume and far-field. However, the procedure will be different and proceeds from a magnetic vector potential formulation.

In order to find the optimal currents on the antenna a optimization method can be used. Gustafsson et al. [15] showed that the amplitude and the phase of a far-field generated by an antenna can be found by convex optimization. In this thesis a genetic optimization algorithm will be used since it is provided by the host company.

1.2 Aim

The aim is to create a calculation-tool which generates the surface currents on a predefined antenna structure for a specified far-field. As mentioned above, the problem is not unique which means that an infinite number of surface current solutions exist, so one challenge is to find the solutions which are physically possible to produce. From physically possible surface currents it is sometimes possible to determine what kind of antenna is suitable. So, a calculation tool could indicate if a theoretical solution exist for the specified volume and the required far-field or not. This could simplify the preliminary stage in the antenna design by giving a direction for the antenna type.

This aim is too broad for this thesis and the objective here is to create a calculation tool in MATLAB where the outline of the antenna and the required far-field can be specified. The program will calculate the far-field for given input parameters, which will be generated by a genetic algorithm optimization [16]. After several iterations the algorithm will find an optimal solution for the given far-field. Then, the theoretical surface currents on the volume will be calculated according to the optimal input parameters.

1.3 Outline

In Ch. 2 the thesis explains the theory, definitions and parameters in order to understand how the far-field is calculated for the specified volume. This chapter is essential in order to understand strengths and weaknesses in the assumptions for the developed MATLAB-tool. Ch. 3 continues with a brief theory for the optimization algorithm that is used in this investigation. The implementation of the code is explained in Ch. 4 followed by the verification of it in Ch 5. The results are presented in Ch. 6 and show the effect of different geometries and restrictions on the far-field. A discussion about the results and their physical feasibility is done in Ch. 7, followed by improvements and suggestions for further work in Ch 8.

Chapter 2

Radiation from a body of revolution

It is common that antennas are rotational symmetric. In this thesis, the volume of the antenna is assumed to be enclosed in a body of revolution (BOR) consisting of cylinders of different dimensions. The BOR is separated into segments according to Fig. 2.1 and the surface can be separated into different regions that represent a lateral area or a base area. The BOR geometry is described in Sec. 2.1. The radiation field from an antenna depends on the surface currents on the body which encloses it, as stated in the equivalence principle in Sec. 2.2. Sec. 2.3 treats the physical equivalent used for calculations of the radiated field for a source close to an infinite ground plane. In Sec. 2.3 the magnetic vector potential is used as a tool in order to find an expression for the electric field, and a far-field approximation is done in Sec. 2.4. The surface currents from Sec. 2.2 are treated in Sec. 2.5. Expressions for the radiated fields from the lateral and base area are stated in Sec. 2.6 and finally, the antenna performance is expressed as directivity in Sec. 2.7.

2.1 Bodies of revolution

The structures that are analysed in this thesis are rotationally symmetric and are usually called bodies of revolution (BOR) [17, Ch.6]. The BOR can represent spheres, ellipsoids and finite cylinders among others. Combinations of the latter are of interest in this work, illustrated in Fig. 2.1. This section gives the basis

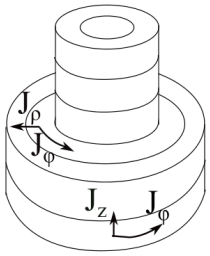

Figure 2.1: Illustration of the BOR that encapsulates the antenna. It is separated into segments and the current densities, J_ρ, J_ϕ, J_z are expressed in cylindrical coordinates.

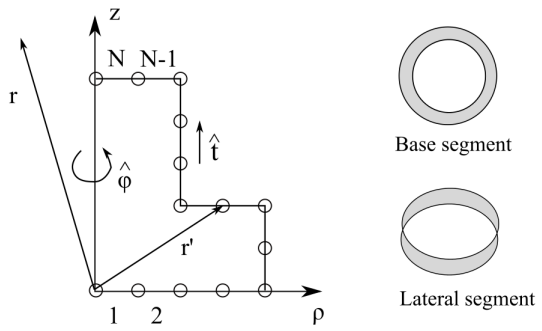

Figure 2.2: Schematically description of the nodes along the t-vector. The segments are formed by a sweep around the z-axis. The structure is the same as the one in Fig. 2.1.

to the construction of the volume structure and presents adequate coordinate systems for representation of source and far-field. Further details about BORs are described by Gibson [17, Ch.6] and vector transformations for coordinate systems are for instance explained by Balanis [18, Ch.II].

The volume structure is defined by nodes that have a ρ- and z-value. A piecewise linear curve with the unit length vector $\hat{\boldsymbol{t}}$ forms a connection between the nodes and generates a closed surface. The nodes divide the body into N segments where each segment forms a circle parallel to the azimuthal vector $\hat{\boldsymbol{\phi}}$. The node placement is shown in Fig. 2.2, where a segment is formed by the area of a sweep between two nodes. The segments parallel to the z-axis are called lateral segments while the ones parallel to the ρ-direction are called base segments. A point on the surface may be represented by cylindrical coordinates (ρ, ϕ, z), by its length variable along the curve and the azimuthal angle (t, ϕ) or in Cartesian coordinates $\boldsymbol{r} = \rho\cos\phi\hat{\boldsymbol{x}} + \rho\sin\phi\hat{\boldsymbol{y}} + z\hat{\boldsymbol{z}}$, $r = |\boldsymbol{r}|$.

Cylindrical coordinates are adequate for describing a BOR consisting of cylindrical segments. The differential displacement is related to the cylindrical coordinates by (2.1).

$$d\boldsymbol{r} = \hat{\boldsymbol{\rho}}d\rho + \hat{\boldsymbol{\phi}}\rho d\phi + \hat{\boldsymbol{z}}dz \tag{2.1}$$

Even though cylindrical coordinates are adequate for the structure it is preferable to represent the electric far-field in spherical coordinates since an antenna radiate spherical waves. Fig. 2.3 shows a cylinder structure in different coordinate systems. Throughout the report, source coordinates located on the cylinder are designated as primed (ρ', ϕ', z') and the observation coordinates located in the far-field as unprimed (r, θ, ϕ).

2.2 Surface equivalence theorem

The surface equivalence theorem states that the field generated inside a volume can be replaced by electric and magnetic surface currents on the boundary of

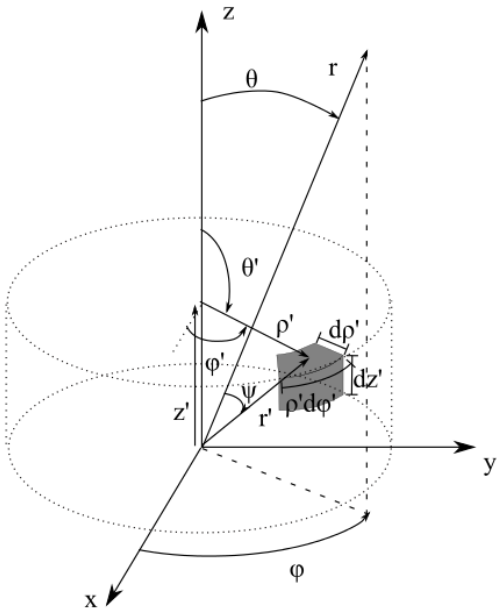

Figure 2.3: Cartesian(x,y,z), cylindrical (ρ, ϕ, z) and spherical (r, θ, ϕ) coordinates for a cylindrical structure.

the volume. This is for example described by Balanis [18, Ch. 7]. The surface equivalence principle makes it possible to look at the surface currents on a structure instead of the actual sources inside it. This will be used in order to define a magnetic vector potential in Sec. 2.4.

Let the real sources $\boldsymbol{J}_1$ and $\boldsymbol{M}_1$ be replaced by equivalent sources within a certain region V_1. The actual fields $\boldsymbol{H}_1$ and $\boldsymbol{E}_1$ outside the imaginary surface S are obtained by suitable electric and magnetic surface currents $\boldsymbol{J}^s$ and $\boldsymbol{M}^s$, respectively. The actual and equivalent cases are schematically shown in Fig. 2.4.

The equivalent source generates the same field outside V_1 as the real source but has a different one inside. The boundary conditions for time-harmonic electromagnetic fields must be fulfilled for the tangential electromagnetic components on S. The surface currents for an equivalent aperture are given by (2.2) and (2.3) for the normal vector $\hat{\boldsymbol{n}}$.

$$\boldsymbol{J}^S = \hat{\boldsymbol{n}} \times (\boldsymbol{H}_1 - \boldsymbol{H}) \tag{2.2}$$

$$\boldsymbol{M}^S = -\hat{\boldsymbol{n}} \times (\boldsymbol{E}_1 - \boldsymbol{E}) \tag{2.3}$$

The fields $\boldsymbol{E}$ and $\boldsymbol{H}$ are not in the region of interest and they may adapt any values. For simplicity, they are assumed to be zero. This form of the surface equivalence theorem is known as Love's equivalence principle. The case may be simplified if the surface coincides with the boundary of a conducting body. Then, the electrical field component vanishes on the surface. In this thesis only electrical sources are considered.

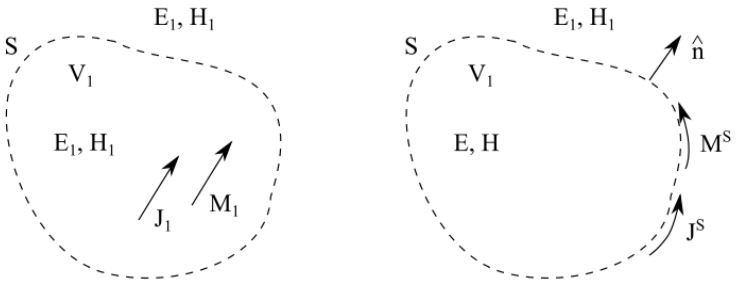

Figure 2.4: The actual sources $\boldsymbol{J}_1$ and $\boldsymbol{M}_1$ generate the fields $\boldsymbol{E}_1$ and $\boldsymbol{H}_1$ everywhere. The currents $\boldsymbol{J}^s$ and $\boldsymbol{M}^s$ are said to be equivalent only outside V_1 since the will produce the same field only outside this volume.

2.3 Electric field

The electric field is of interest in order to calculate the intensity of the far-field. One way to express the electric field is presented in (2.4) for the electric potential ϕ_e, magnetic vector potential $\boldsymbol{A}$ and angular frequency ω [18, Ch. 6].

$$\boldsymbol{E} = -\mathrm{j}\omega\boldsymbol{A} - \nabla\phi_e \tag{2.4}$$

By adopting Lorenz gauge condition (2.5) for the divergence of the magnetic vector potential, the Helmholtz wave equation (2.6) may be obtained. Here ϵ is the permittivity, μ is the permeability and k is the the wave number, $k = \omega\sqrt{\mu\epsilon}$.

$$\nabla \cdot \boldsymbol{A} = -\mathrm{j}\omega\epsilon\mu\phi_e \quad \text{(Lorenz gauge condition)} \tag{2.5}$$

$$\nabla^2\boldsymbol{A} + k^2\boldsymbol{A} = -\mu\boldsymbol{J} \quad \text{(Helmholtz wave equation)} \tag{2.6}$$

The solution to Helmholtz's wave equation (2.6) gives the magnetic vector potential, (2.7). For a more detailed description see [18, Ch. 6].

$$\boldsymbol{A}(\boldsymbol{r}) = \frac{\mu}{4\pi}\iint_S \boldsymbol{J}^S(\boldsymbol{r'})\frac{e^{-\mathrm{j}k|\boldsymbol{r}-\boldsymbol{r'}|}}{|\boldsymbol{r}-\boldsymbol{r'}|}dS(\boldsymbol{r'}) \tag{2.7}$$

The magnetic vector potential depends on the observation and the source point, $\boldsymbol{r}$ and $\boldsymbol{r'}$, respectively, which is illustrated in Fig. 2.5. The surface S encloses the linear current densities which are nonzero and dS' is an infinitesimal section on the surface.

Since antennas of finite size radiate spherical waves, the scattered electrical field is often represented in spherical coordinates. In this case, the radiation body is of cylindrical shape and therefore it is advantageous to use cylindrical coordinates for representing the surface, while the radiated field is in spherical coordinates.

The magnetic vector potential is separated into spherical directions. The r variations are separable from those of θ and ϕ and the amplitude dependence is

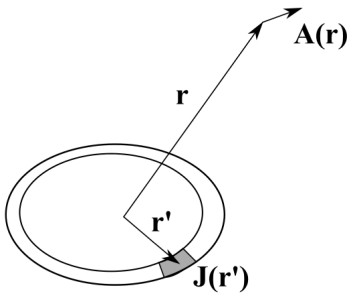

Figure 2.5: The current density $\boldsymbol{J}$ at the source point $\boldsymbol{r'}$ gives a magnetic vector potential $\boldsymbol{A}$ at the observation point $\boldsymbol{r}$

the same for all directions in this coordinate system, $1/r^n$ for $n = 1, 2\ldots$ For the far- field, higher order terms are neglected and the magnetic vector potential takes the form of (2.8) [18, Ch. 6]. Note that $\boldsymbol{A}$ and A_r, A_θ, A_ϕ have different units due to the trailing far field factor e^{-jkr}/r in (2.8).

$$\boldsymbol{A} = \Big[\hat{\boldsymbol{r}}A_r(\theta,\phi) + \hat{\boldsymbol{\theta}}A_\theta(\theta,\phi) + \hat{\boldsymbol{\phi}}A_\phi(\theta,\phi)\Big]\frac{e^{-\mathrm{j}kr}}{r} \qquad r \to \infty \tag{2.8}$$

The electric field in (2.4) is expressed with the magnetic vector potential and the electric scalar potential. By utilising Lorenz gauge condition (2.5) an expression for the electric field only dependent on the magnetic vector potential is obtained as (2.9).

$$\boldsymbol{E} = -j\omega\boldsymbol{A} - j\frac{1}{\omega\mu\epsilon}\nabla(\nabla\cdot\boldsymbol{A}) \tag{2.9}$$

Substituting (2.8) into (2.9) reduces it to (2.10). It can be seen that the first and second term of (2.10) in the radial direction cancel out. Once again higher order terms of $1/r^n$ are neglected for the far-field which results in (2.11). The assumption that higher order terms of $1/r^n$ are neglected means that the term for the magnetic vector potential in r-direction is negligible compared to the ones in θ- and ϕ-direction [18, Ch. 6].

$$\begin{aligned}\boldsymbol{E} &= \frac{1}{r}\Big(-\mathrm{j}\omega e^{-\mathrm{j}kr}\Big[\hat{\boldsymbol{r}}A_r(0) + \hat{\boldsymbol{\theta}}A_\theta(\theta,\phi) + \hat{\boldsymbol{\phi}}A_\phi(\theta,\phi)\Big]\Big)\\ &\quad + \frac{1}{r^2}\Big(\ldots\Big) + \ldots\end{aligned} \tag{2.10}$$

$$\left.\begin{aligned}E_r &= 0\\ E_\theta &= -\mathrm{j}\omega A_\theta\tfrac{e^{-\mathrm{j}kr}}{r}\\ E_\phi &= -\mathrm{j}\omega A_\phi\tfrac{e^{-\mathrm{j}kr}}{r}\end{aligned}\right\}\ \boldsymbol{E}_{\theta,\phi} = -\mathrm{j}\omega\boldsymbol{A}_{\theta,\phi}\frac{e^{-\mathrm{j}kr}}{r} \tag{2.11}$$

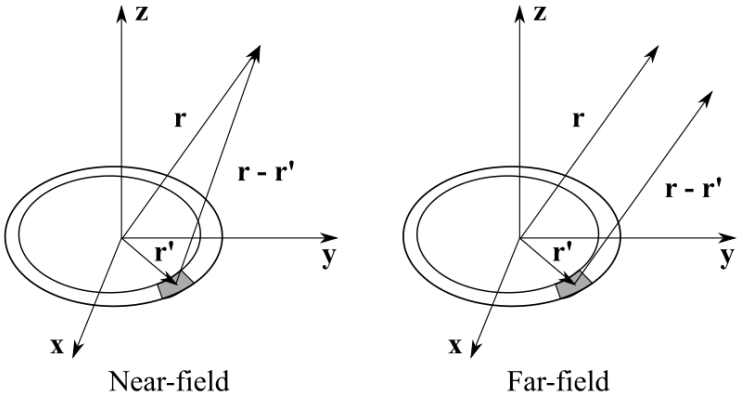

Figure 2.6: Illustration of near- and far-field geometry

2.4 Far-field

The near- and far-field geometry is show in Fig 2.6. The far-field approximation assumes that the field point $\boldsymbol{r}$ is very far from the current source $\boldsymbol{r'}$. Hence, in the far zone $|\boldsymbol{r}| \gg |\boldsymbol{r'}|$ and $|k\boldsymbol{r}| \gg 1$ $|kr| \gg 1$, see [7, Ch. 5]. It can be seen that the distance between the observation and source point is approximated by r whereas the phase between them is approximated by $r - \hat{\boldsymbol{r}} \cdot \boldsymbol{r'}$, (2.12) - (2.14).

$$
\begin{aligned}
|\boldsymbol{r} - \boldsymbol{r'}| &\simeq r - \hat{\boldsymbol{r}} \cdot \boldsymbol{r'} && (2.12)\\
\hat{\boldsymbol{r}} \cdot \boldsymbol{r'} &= (\rho' \cos\phi' \hat{\boldsymbol{x}} + \rho' \sin\phi' \hat{\boldsymbol{y}} + z' \hat{\boldsymbol{z}}) \\
&\quad \cdot(\sin\theta\cos\phi\hat{\boldsymbol{x}} + \sin\theta\sin\phi\hat{\boldsymbol{y}} + \cos\theta\hat{\boldsymbol{z}}) \\
&= \rho' \sin\theta\cos(\phi - \phi') + z'\cos\theta && (2.13)\\
\frac{e^{-\mathrm{j}k|\boldsymbol{r}-\boldsymbol{r'}|}}{|\boldsymbol{r}-\boldsymbol{r'}|} &\rightarrow \frac{e^{-\mathrm{j}kr}}{r} e^{\mathrm{j}k\boldsymbol{r'}\cdot\hat{\boldsymbol{r}}} && (2.14)
\end{aligned}
$$

Hence, a general expression for the electric far-field (2.15) is derived by inserting the magnetic vector potential (2.7) into the electric field (2.11) and adapt the approximation from (2.14). Only the current surface components perpendicular to $\hat{\boldsymbol{r}}$ are considered, $\boldsymbol{J}_t^S$.

$$
\boldsymbol{E}(\boldsymbol{r}) = -\frac{\mathrm{j}\omega\mu}{4\pi}\frac{e^{-\mathrm{j}kr}}{r}\iint_S \boldsymbol{J}_t^S(\boldsymbol{r'}) e^{\mathrm{j}k\boldsymbol{r'}\cdot\hat{\boldsymbol{r}}} dS(\boldsymbol{r'}) \qquad (2.15)
$$

2.5 Surface current

The surface current is preferably expressed in cylindrical coordinates since the structure is of cylindrical shape. The radiating waves in turn are of spherical shape. Therefore the surface current is expressed in cylindrical coordinates while the coordinate directions are spherical.

The surface current is described by (2.16) for Cartesian coordinates. The current components J_x, J_y, J_z can be written in spherical coordinates as (2.17) - (2.19) and unit vectors $\hat{\boldsymbol{x}}, \hat{\boldsymbol{y}}, \hat{\boldsymbol{z}}$ in spherical coordinates are given by (2.20) - (2.22).

$$\boldsymbol{J}^S = \hat{\boldsymbol{x}} J_x + \hat{\boldsymbol{y}} J_y + \hat{\boldsymbol{z}} J_z \tag{2.16}$$

$$\begin{aligned} J_x &= J_\rho \cos\phi - J_\phi \sin\phi && (2.17)\\ J_y &= J_\rho \sin\phi + J_\phi \cos\phi && (2.18)\\ J_z &= J_z && (2.19) \end{aligned}$$

$$\begin{aligned} \hat{\boldsymbol{x}} &= \hat{\boldsymbol{r}} \sin\theta\cos\phi + \hat{\boldsymbol{\theta}} \cos\theta\cos\phi - \hat{\boldsymbol{\phi}} \sin\phi && (2.20)\\ \hat{\boldsymbol{y}} &= \hat{\boldsymbol{r}} \sin\theta\sin\phi + \hat{\boldsymbol{\theta}} \cos\theta\sin\phi + \hat{\boldsymbol{\phi}} \cos\phi && (2.21)\\ \hat{\boldsymbol{z}} &= \hat{\boldsymbol{r}} \cos\theta - \hat{\boldsymbol{\theta}} \sin\theta && (2.22) \end{aligned}$$

Rewriting of (2.16) with (2.17) - (2.22) gives the surface current in spherical coordinates. For a better survey the surface current is separated it into ρ-, θ- and ϕ-directions in (2.23) - (2.25). Inserting $\boldsymbol{J}_\theta^S$ and $\boldsymbol{J}_\phi^S$ into (2.15) gives the E_θ and E_ϕ, respectively [18].

$$\begin{aligned} J_r^S &= J_\rho \sin\theta\cos(\phi-\phi') + J_\phi \sin\theta\sin(\phi-\phi') + J_z\cos\theta && (2.23)\\ J_\theta^S &= J_\rho \cos\theta\cos(\phi-\phi') + J_\phi \cos\theta\sin(\phi-\phi') - J_z\sin\theta && (2.24)\\ J_\phi^S &= -J_\rho \sin(\phi-\phi') + J_\phi \cos(\phi-\phi') && (2.25) \end{aligned}$$

J_ρ, J_ϕ and J_z are the currents in corresponding coordinate directions. The trigonometrical functions $\cos(m\phi)$ and $\sin(m\phi)$ will be able to generate any solution for the these currents. Different angles are allowed in the source and observation systems (ϕ' and ϕ) and $\boldsymbol{z}'$ is fixed. Hence, an ansatz for the surface currents is assumed as (2.26) - (2.28) for complex constants B_m and D_m for mode number m.

$$J_\rho = \sum_{m=0}^{M} B_m^\rho \cos(m\phi') + D_m^\rho \sin(m\phi') \qquad 0 \text{ for lateral surface} \tag{2.26}$$

$$J_\phi = \sum_{m=0}^{M} B_m^\phi \cos(m\phi') + D_m^\phi \sin(m\phi') \tag{2.27}$$

$$J_z = \sum_{m=0}^{M} B_m^z \cos(m\phi') + D_m^z \sin(m\phi') \qquad 0 \text{ for base surface} \tag{2.28}$$

2.6 Radiated field

As mentioned before, the BOR is separated into two different kinds of surfaces, the lateral and the base area. The radiated electric fields are specified separately for those parts.

2.6.1 Lateral surface

For the lateral surface the current flows in ϕ- and z-direction, i.e. $J_\rho = 0$, moreover ρ' adopts the value of the radius. In this way the electric field becomes (2.29) and (2.30) for the constant $K = -\frac{\mathrm{j}\omega\mu}{\pi}\frac{e^{-\mathrm{j}kr}}{r}$. The currents J_ϕ and J_z are specified in (2.27) and (2.28), respectively.

$$E_\theta^{lat} = K \iint (J_\phi \cos\theta \sin(\phi - \phi') - J_z \sin\theta) e^{\mathrm{j}k\boldsymbol{r'}\cdot\hat{\boldsymbol{r}}} \rho' d\phi' dz' \tag{2.29}$$

$$E_\phi^{lat} = K \iint J_\phi \cos(\phi - \phi') e^{\mathrm{j}k\boldsymbol{r'}\cdot\hat{\boldsymbol{r}}} \rho' d\phi' dz' \tag{2.30}$$

2.6.2 Base surface

For the base area the current flows in ρ- and ϕ-direction, i.e. $J_z = 0$. In this way the electric field become (2.31) and (2.32) for the constant $K = -\frac{\mathrm{j}\omega\mu}{\pi}\frac{e^{-\mathrm{j}kr}}{r}$. The currents J_ρ and J_ϕ are specified in (2.26) and (2.27), respectively.

$$E_\theta^{base} = K \iint (J_\rho \cos\theta \cos(\phi - \phi') + J_\phi \cos\theta \sin(\phi - \phi')) e^{\mathrm{j}k\boldsymbol{r'}\cdot\hat{\boldsymbol{r}}} \rho' d\rho' d\phi' \tag{2.31}$$

$$E_\phi^{base} = K \iint (-J_\rho \sin(\phi - \phi') + J_\phi \cos(\phi - \phi')) e^{\mathrm{j}k\boldsymbol{r'}\cdot\hat{\boldsymbol{r}}} \rho' d\rho' d\phi' \tag{2.32}$$

2.7 Radiation intensity

When discussing antenna performance, one usually discusses gain in decibel (dB) units. These antenna definitions are defined by the Antenna Standards Committee [19] and are treated by Balanis [20, Ch.1]. A brief summary of the most important parameters regarding intensity measurements is presented.

The radiation intensity is the angular distribution of the radiated power around the antenna. In a given direction it is defined as the power radiating from the antenna per steradian. A steradian is the measure of the solid angle. A solid angle of one steradian, on its part, constitutes the angle which gives an area of r^2 on the surface for a sphere of radius r, see Fig 2.7. The radiation intensity for the far-field is approximated as (2.33), where η is the intrinsic impedance of the medium. The total radiated power is given by (2.34).

$$U(\theta, \phi) = \lim_{r\to\infty} \frac{r^2}{2\eta} |\boldsymbol{E}(r, \theta, \phi)|^2 \tag{2.33}$$

$$P_{rad} = \int_0^{2\pi} \int_0^{\pi} U(\theta, \phi) \sin\theta d\theta d\phi \tag{2.34}$$

The directivity is the radiation intensity normalized by the average intensity. This

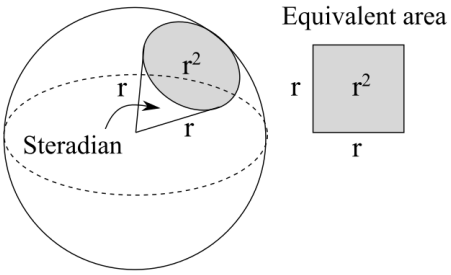

Figure 2.7: Illustration of a steradian.

means that it is a measure of how"directional" the antenna is. The directivity is given by (2.35).

$$D = \frac{4\pi U}{P_{rad}} \tag{2.35}$$

When the directivity is expressed in dB-scale it can be done relative to different reference levels. (2.35) correspond to an isotropic radiation reference level, which is expressed as dBi.

Polarization describes how the electric field is composed and propagates. If the electric field oscillates in one single direction it is said to be linearly polarized. If the electric field has two perpendicular components that are not in phase it is said to be elliptically polarized. The special case when the magnitude of both the perpendicular components are equal and out of phase with a phase shift of 90° is called circular polarized. Any other case would be called an elliptically polarized wave, and could be either right hand polarized or left hand polarized. The electric field in (2.33) could have different polarizations. The linearly(lin), right hand circular (RHC) and left hand circular (LHC) polarized cases for spherical coordinates are shown in (2.36)-(2.38) [21].

$$|\boldsymbol{E}_{lin}(\theta,\phi)|^2 = |E_\theta|^2 + |E_\phi|^2 \tag{2.36}$$

$$|\boldsymbol{E}_{RHC}(\theta,\phi)|^2 = \frac{1}{2}|E_\theta + \mathrm{j}E_\phi|^2 \tag{2.37}$$

$$|\boldsymbol{E}_{LHC}(\theta,\phi)|^2 = \frac{1}{2}|E_\theta - \mathrm{j}E_\phi|^2 \tag{2.38}$$

An antenna is never 100% polarized in one single mode. Therefore radiation patterns for two different polarizations are of interest: the co-polarized radiation pattern and the cross polarized radiation pattern. The co-polarized electric field is the polarization of interest and the cross-polarization is orthogonal to that one. For example, if an antenna will radiate a RHC electric field this is the co-polarized component, while the LHC electric field is the cross polarized component.

Chapter 3
Optimization

Optimization is a systematic decision making process where the goal is to find the best solution among many feasible solutions that are available. The evolution process in nature reveals that it follows optimization. For example, hares living in the north get a white winter coat whereas hares in the south do not. Inspired by the evolution process evolution optimization algorithms have been developed [22], [23]. Simple algorithms for solving optimization problems can start at an initial single point in the search space. Through a sequence of computational steps, the optimal solution can be found through the gradient. This kind of optimization has a risk of finding a local minimum instead of the global one. In order to avoid this, a population approach is used for the genetic algorithm [16].

3.1 Genetic algorithm

The genetic algorithm is one of the most widely known evolutionary algorithms used today. The evolutionary algorithms imitate the reproduction of living beings, which have a natural evolutionary process, and presents a stochastic optimization technique. The interest in this optimization technique started in the 1960s and has increased since then. The genetic algorithm is described by Gen et al [16].

The Genetic Algorithm starts with a population. A population consists of a random set of solutions, also called chromosomes, which have genes, a string of values. They satisfy the boundary and system constraints to the optimization problem. The population experiences a simulated evolution where the chromosomes evolve through iterations, also called generations. New chromosomes, called offsprings, are created by two chromosomes from the current version becoming a hybrid, so called "crossover", or by changing the value of one or several genes, so called "mutation". The new generation is created by selection from the present version and the offsprings. The selection is performed according to a fitness value, which is evaluated after each generation; fitter chromosomes have a higher probability of being selected. The ones that are not selected are rejected. In this way, the algorithms converge to a better chromosome. A flow-chart for the genetic algorithm is illustrated in Fig. 3.1.

The genetic algorithm combines directed and stochastic search in order to explore the search space and exploit the best solution. At the beginning of each optimization the population is diverged. In the first generations the offsprings

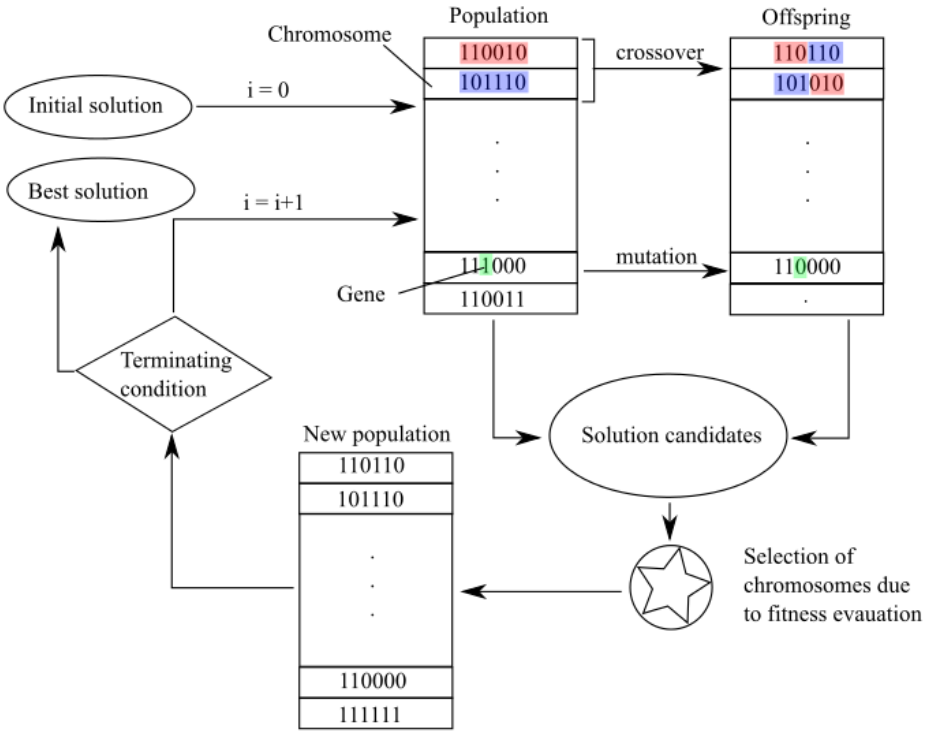

Figure 3.1: Flow-chart for the genetic algorithm.

exploit all solution space, and when the solution converges the offsprings exploit the neighborhood of each chromosome.

Usually three major advantages are highlighted in connection to the genetic algorithm; the adaptability, the robustness and the flexibility. The algorithm is adaptable to any kind of objective functions as well as any kind of constraints. In general the optimization method is more efficient and more robust in locating optimal solutions and reducing computational effort than methods utilising the gradient. Finally, the implementation is efficient due to the flexibility of the hybridization of the domain-dependent heuristics.

3.2 RUAG implementation of genetic algorithms

RUAG has an in house implemented genetic algorithm which was used in this thesis work. It is a MATLAB script that works generally and combines simplex and randomly predicted search. In order to run the software a cost function needs to be defined by the user and written in a specific subroutine which return a cost value. This thesis intends to provide this cost function.

An input data file includes all information for the optimization conditions, such as population size, number of unknowns and parameter range for them, convergence criteria and percentage of old population which will be replaced by offspring.

The optimization can be performed with two ways. The first one has one set of optimizations and a population size of 30 times the number of unknowns. The convergence criteria is set to a predefined number of iterations without improvement or a certain parameter spread. The second one has automatic restarts of the set of optimizations, where the allowed parameter range is refreshed according to the until now best optimization. With automatic restarts the population size can be smaller, five times the number of unknown. The convergence criteria is set to a maximum number of iterations.

Chapter 4

Implementation

The code was implemented with MATLAB which is a multi-paradigm numerical computing environment [24]. Except for the optimization algorithm, the MATLAB-tool was developed from scratch with the theory from Ch. 2. The code was separated into two different parts. The first part defined parameters and calculated basis functions, whereas the second part was connected to the optimization algorithm for cost evaluation.

The first part was run before the main program in order to set constants, structure, current basis functions and mask. With this information it calculated the radiated field from the magnetic vector potential basis functions that were used in the second part for the field calculations. Regarding the structure, the nodes build up segments and were defined in cylindrical coordinates (ρ, z). The mask, current basis functions and magnetic potential basis functions are explained in greater detail in Sec. 4.1 - 4.3.

The second part of the developed code was connected to the optimization algorithm explained in Sec. 3.1. The adaptation of the optimization algorithm is described in Sec. 4.4. The MATLAB-tool calculated the electric field and thereby the intensity distribution. The cost evaluation is explained in 4.5 and the values were returned to the optimization algorithm. Finally, the surface currents were calculated for a three dimensional structure in Sec. 4.6.

4.1 Mask definition

A mask defines the allowed directivity for different elevation angles for the radiated far-field. A mask was constructed in order to be used for the optimization. Maximum and minimum directivity for the output intensity were defined for certain elevation angles in θ-direction. These angles were used for the cost-calculations (see Sec. 4.5), thus the cost accuracy was determined by the distance between the defined angles. Fig. 4.1 and Tab 4.1 show an example of the minimum and maximum values for different angles. The masks for the co- and the cross- polarization were defined separately and are displayed in the same graph.

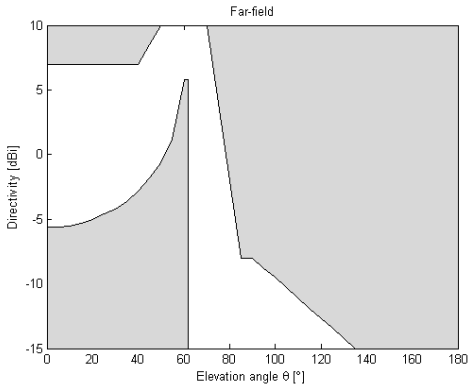

Figure 4.1: Example of a mask, allowed range for the co-polarized field is within the white zone while the allowed one for the cross-polarized field is below -15dBi. The values correspond to Tab. 4.1.

Table 4.1: Example of mask construction with minimum and maximum directivity for different angles, the values correspond to Fig. 4.1.

Elevation angle [deg]	0	5	10	···	60	62	···	180
Min directivity [dBi]	-5.6	-5.6	-5.5	···	5.8	5.8	···	-inf
Max directivity [dBi]	7.0	7.0	7.0	···	10.0	10.0	···	-15

4.2 Current basis functions

The currents for the cylindrical directions are given by (2.26) - (2.28) and are repeated here for convenience (4.1) - (4.3).

$$J_\rho = \sum_{m=0}^{M} B_m^\rho \cos(m\phi') + D_m^\rho \sin(m\phi') \qquad 0 \text{ for lateral surface} \tag{4.1}$$

$$J_\phi = \sum_{m=0}^{M} B_m^\phi \cos(m\phi') + D_m^\phi \sin(m\phi') \tag{4.2}$$

$$J_z = \sum_{m=0}^{M} B_m^z \cos(m\phi') + D_m^z \sin(m\phi') \qquad 0 \text{ for base surface} \tag{4.3}$$

The currents were assumed to be sums of several modes of the trigonometrical cosine and sine functions. A higher mode gives more oscillations of the current per wavelength and in practice it is not possible to have too many. Therefore, the number of modes could change for the ρ- ϕ- and z-directions, dependent on the dimension of the structure. The current basis functions were saved as strings in a cell array; this is illustrated in Tab. 4.2.

Table 4.2: The current basis functions were saved as strings in one cell array for each direction, J_ρ, J_ϕ and J_z, respectively.

mode	$\cos(m\phi')$	$\sin(m\phi')$
0	'1'	'0'
1	'$\cos(\phi')$'	'$\sin(\phi')$'
2	'$\cos(2 \cdot \phi')$'	'$\sin(2 \cdot \phi')$'
...	...	...

4.3 Magnetic vector potential basis functions

Each unknown variable, B_m and D_m in (4.1) - (4.3) received two magnetic vector potential basis functions, one for the θ- and one for the ϕ-direction. This is illustrated in Tab. 4.3. The current basis functions were repeated for all three directions since they were different for each of them. This means that each segment could have six unknown parameters and a magnetic vector potential in θ-direction with six contributing terms and in ϕ-direction four contributing terms.

If the magnetic vector potential in (2.7) is written with the far-field approximation from (2.14), it takes the form of (4.4).

$$\boldsymbol{A}(\boldsymbol{r}) = \frac{\mu}{4\pi} \iint_S \boldsymbol{J}^S(\boldsymbol{r'}) \frac{e^{-\mathrm{j}kr}}{r} e^{\mathrm{j}k\boldsymbol{r'}\cdot\hat{\boldsymbol{r}}} dS(r') \tag{4.4}$$

Table 4.3: Surface current $\boldsymbol{J}^S(\boldsymbol{r'})$.

unknown variable	current basis function	surface current, J_θ^S, J_ϕ^S
$B_{\theta m}^{\rho}$	$\cos(m\phi')$	$\cos\theta\cos(\phi-\phi')$
$D_{\theta m}^{\rho}$	$\sin(m\phi')$	
$B_{\phi m}^{\rho}$	$\cos(m\phi')$	$(-1)\sin(\phi-\phi')$
$D_{\phi m}^{\rho}$	$\sin(m\phi')$	
$B_{\theta m}^{\phi}$	$\cos(m\phi')$	$\cos\theta\sin(\phi-\phi')$
$D_{\theta m}^{\phi}$	$\sin(m\phi')$	
$B_{\phi m}^{\phi}$	$\cos(m\phi')$	$\cos(\phi-\phi')$
$D_{\phi m}^{\phi}$	$\sin(m\phi')$	
$B_{\theta m}^{z}$	$\cos(m\phi')$	$(-1)\sin\theta$
$D_{\theta m}^{z}$	$\sin(m\phi')$	
$B_{\phi m}^{z}$	$\cos(m\phi')$	0
$D_{\phi m}^{z}$	$\sin(m\phi')$	

The different terms of the magnetic vector potential (4.4) inside the integral were written as strings and combined with an inline function. The three different parts that compose the inline function were:

- The cosine or sine term for mode m from Tab. 4.3.
- The surface current J_θ^S or J_ϕ^S from Tab. 4.3.
- $e^{\mathrm{j}k\hat{\boldsymbol{r}}\cdot\boldsymbol{r'}}$

$\frac{e^{-\mathrm{j}kr}}{r}$ from the expression in (4.4) was excluded since it is the same for all elements and acts only as a magnification term.

Two magnetic vector potential matrices, one for the θ- and one for the ϕ-direction, with one basis function for each unknown, were created by going through the current basis functions described in Sec. 4.2. For each segment there was a loop over all the modes for all current directions. If the current basis function was set to zero, no magnetic vector potential basis function was received. This is illustrated in the flow-chart in Fig. 4.2 and Fig. 4.3. A magnetic vector potential basis function matrix $\boldsymbol{A}_\theta$ is shown in (4.5) and one row vector with the basis functions in (4.6). The first superscript stands for the direction of the assigned current, i.e. ρ, ϕ or z. The second superscript indicates the segment number. The first subscript indicates if it is the cosine (B) or sine (D) term. Finally, the second subscript specifies the mode number.

$$\boldsymbol{A}_\theta = \begin{bmatrix} \boldsymbol{A}_{\theta 1} \\ \boldsymbol{A}_{\theta 2} \\ \boldsymbol{A}_{\theta 3} \\ \cdots \end{bmatrix} \tag{4.5}$$

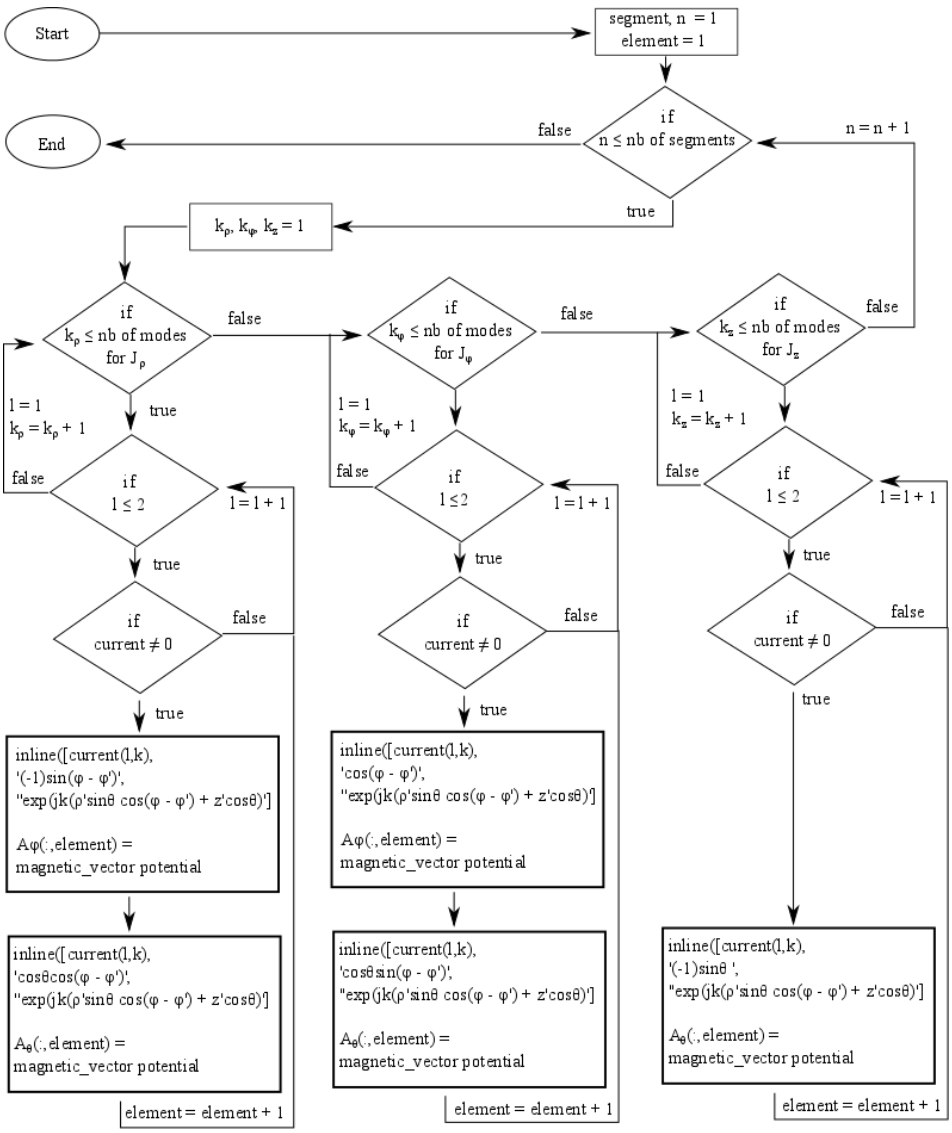

Figure 4.2: Flow-chart for the main part of the program for the magnetic vector potential basis functions, which are generated as two matrices $\boldsymbol{A}_\rho$ and $\boldsymbol{A}_\theta$. The magnetic vector potential calculation is shown in Fig. 4.3. The loaded files for this function are the variables, constants, structure, current basis functions and the mask.

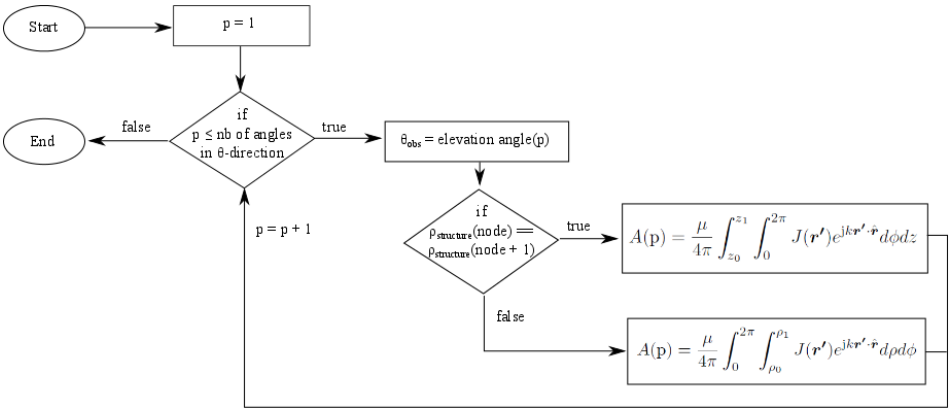

Figure 4.3: Flow-chart for the magnetic vector potential $\boldsymbol{A}$, which is given by the integral 4.4. The loaded data for this calculations are the constants, structure and the mask.

$$\boldsymbol{A}_{\theta 1} = \begin{bmatrix} A_{B0}^{\rho 1} & A_{D0}^{\rho 1} & A_{B1}^{\rho 1} & A_{D1}^{\rho 1} & A_{B0}^{\phi 1} & A_{D0}^{\phi 1} & \cdots & A_{B0}^{\rho 2} & A_{D0}^{\rho 2} & \cdots \end{bmatrix} \tag{4.6}$$

Each row in the $\boldsymbol{A}_{\theta}$- matrix was calculated for a specific θ, decided by the mask in Sec. 4.1. As can be seen in (4.4), the magnetic vector potential is an integral over the surface, it is calculated by the inbuilt MATLAB function integral2. In order to decide if it was the lateral area or the base area which should be integrated, the program checked if the two node points in the ρ-direction for the structure were equal or not. If they were, it was a lateral segment and otherwise it was a base segment.

4.4 Adaptation of optimization algorithm

The optimization algorithm generated solution proposals which were sent to the MATLAB tool which returned the cost for the given solutions. In turn the optimization program generated new proposed solutions. This was repeated as several iterations where the next generation depended on the previous one. The number of iterations were decided by the convergence criteria, which were chosen in the optimization program as:

- a maximum number of iterations
- a maximum parameter spread or a chosen number of iterations without improvement

When the convergence criteria were reached, new limits were calculated for the maximum and minimum values and the process started over again. The process is illustrated as a flow-chart in Fig 4.4.

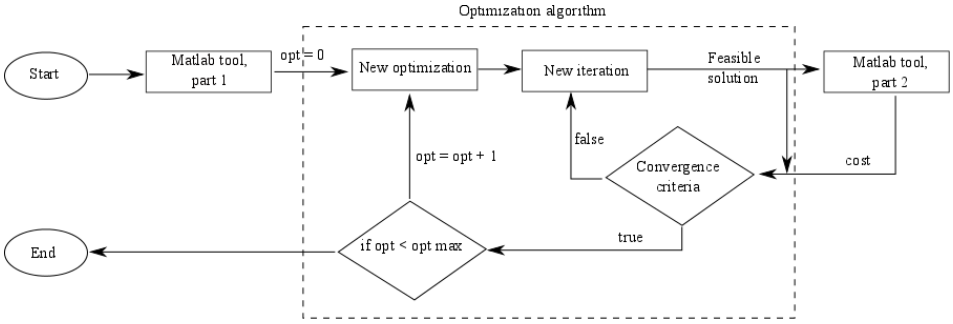

Figure 4.4: Flow-chart for the adaption of the optimization algorithm to the MATLAB-tool.

4.5 Cost evaluation

It is the cost that determines how good a population is and if it is better or worse than the previous ones.

The cost was evaluated in the points for the defined evaluation angles in the mask. If the directivity for one angle was within the mask, i.e. within the white area, the cost was set to zero. For a directivity above or below the mask a cost of the absolute value for the difference was achieved, see Fig. 4.5. The cost was calculated as the sum of the differences between the mask and the generated radiation pattern in dB scale, if it is outside the allowed range. The cost function is presented in (4.7) where p is the number of angles in θ-direction. The first sum represent the cost for the directivity for the right hand circular polarization and the second sum represent the cost the directivity for the left hand circular polarization.

$$\begin{aligned}\text{cost} = &\sum_{p=1}^{N_\theta} \begin{cases} \text{mask}_{\text{min}}^{\text{RHC}}(p) < \text{RHC}(p) < \text{mask}_{\text{max}}^{\text{RHC}}(p), & \text{cost}(p) = 0 \\ \text{RHC}(p) < \text{mask}_{\text{min}}^{\text{RHC}}(p), & \text{cost}(p) = \text{mask}_{\text{min}}^{\text{RHC}}(p) - \text{RHC}(p) \\ \text{mask}_{\text{max}}^{\text{RHC}}(p) < \text{RHC}(p), & \text{cost}(p) = \text{RHC}(p) - \text{mask}_{\text{max}}^{\text{RHC}}(p) \end{cases} \\ + &\sum_{p=1}^{N_\theta} \begin{cases} \text{mask}_{\text{min}}^{\text{LHC}}(p) < \text{LHC}(p) < \text{mask}_{\text{max}}^{\text{LHC}}(p), & \text{cost}(p) = 0 \\ \text{LHC}(p) < \text{mask}_{\text{min}}^{\text{LHC}}(p), & \text{cost}(p) = \text{mask}_{\text{min}}^{\text{LHC}}(p) - \text{LHC}(p) \\ \text{mask}_{\text{max}}^{\text{LHC}}(p) < \text{LHC}(p), & \text{cost}(p) = \text{LHC}(p) - \text{mask}_{\text{max}}^{\text{LHC}}(p) \end{cases} \end{aligned} \tag{4.7}$$

The generated radiation pattern was calculated by multiplying the suggested solution from the optimization program B, D in Tab. 4.3 with the electric field from (2.15); this gave (4.8). K is a vector containing the proposed solutions for the unknown variables B, D. The directivity was then calculated in accordance with Sec. 2.7.

$$\boldsymbol{E}_{\theta,\phi} = -\mathrm{j}\omega \boldsymbol{K} \boldsymbol{A}_{\theta,\phi} \tag{4.8}$$

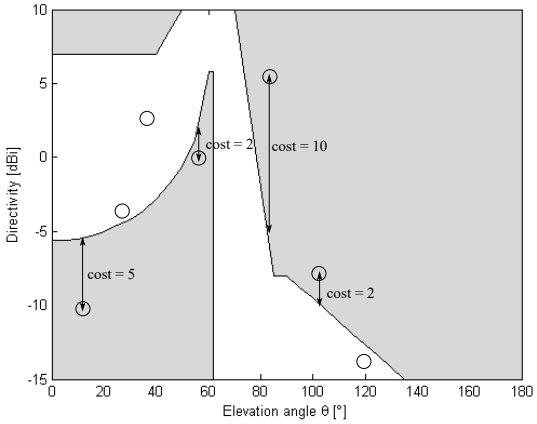

Figure 4.5: The cost is calculated as the sum of the differences between the radiated pattern and the mask. The cost within the mask, white area, is zero.

4.6 Surface currents

The optimization algorithm generated coefficients for the basis functions for the magnetic vector potential. In order to find the surface currents the coefficient was multiplied with its proper current Ansatz given in Tab. 4.2. This was performed for all segments and a number of angles in the ϕ-direction in order to show a three dimensional current distribution. The code for the looping through the segments and currents is illustrated in Fig. 4.6, and has the same structure as the one for the magnetic vector potential basis functions. Compare the flow-charts to see the similarities.

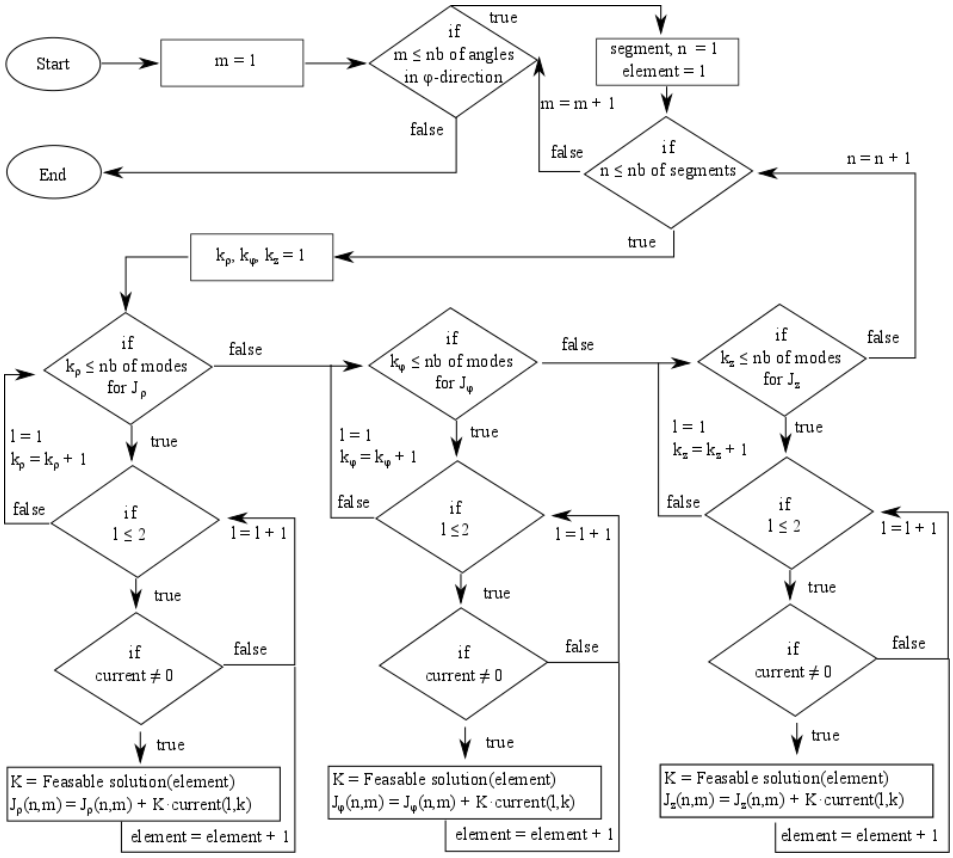

Figure 4.6: Flow-chart for surface current calculation, loaded data are the variables, structure, current basis function and the suggested solution coefficients K.

Chapter 5
Verification

The MATLAB-tool needed to be verified with known data in order to check that it delivered correct results. This was essential in order to assure that the generated results were trustworthy. A verification determines if the program is correctly implemented. The verification was performed by comparing the output data with known results for a dipole and a circular loop. The validation data are taken from Balanis [7] and Werner [25].

5.1 Dipole

A dipole is a thin cylinder where the currents in ρ- and ϕ-directions can be approximated as zero, since the wavelength of the radiated field is much larger than the diameter and circumference. The verification data assumes zero radius and a center-fed dipole where the current vanishes at the endpoints. This current distribution is expressed as (5.1) for the current I_0, wavenumber k, and length l. A graphical illustration can be seen in Fig 5.1.

$$\boldsymbol{I}(\rho', \phi', z') = \begin{cases} \hat{\boldsymbol{z}} I_0 \sin\left[k\left(\frac{l}{2} - z'\right)\right], & 0 \leq z' \leq l/2 \\ \hat{\boldsymbol{z}} I_0 \sin\left[k\left(\frac{l}{2} + z'\right)\right], & -l/2 \leq z' \leq 0 \end{cases} \tag{5.1}$$

The radiation pattern depends on the length of the dipole. For a small dipole the radiation pattern is broad and donut shaped. When the length of the dipole increases the beam becomes more narrow, and when the length of it is beyond one wavelength the number of lobes increase. The radiation intensity for a thin dipole is given by (5.2) for the intrinsic impedance η. The radiation pattern is shown in Fig. 5.2 for a dipole with length $\lambda/2$, λ, and $3\lambda/2$, respectively [7, Ch.4].

$$U = \eta \frac{|I_0|^2}{8\pi^2} \left[\frac{\cos\left(\frac{kl}{2}\cos\theta\right) - \cos\left(\frac{kl}{2}\right)}{\sin\theta} \right]^2 \tag{5.2}$$

A cylinder with radius of $10^{-8}\lambda$ is created in the program and is separated into 35 segments. A sinusoidal current in accordance with (5.1) is sampled in the middle of each segment. The normalized radiation patterns for a dipole of length $\lambda/2$, λ, and $3\lambda/2$, respectively, are shown in Fig. 5.2. A visual comparison between the generated one and the reference shows small deviations for low directivities.

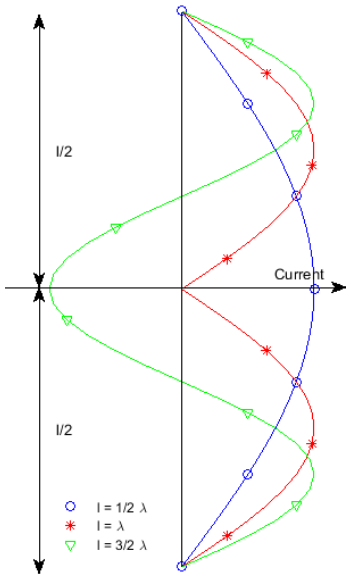

Figure 5.1: Sinusoidal current distribution on a center-fed dipole of three different lengths: $l = \lambda/2$, λ, and $3\lambda/2$. The current direction changes between positive and negative.

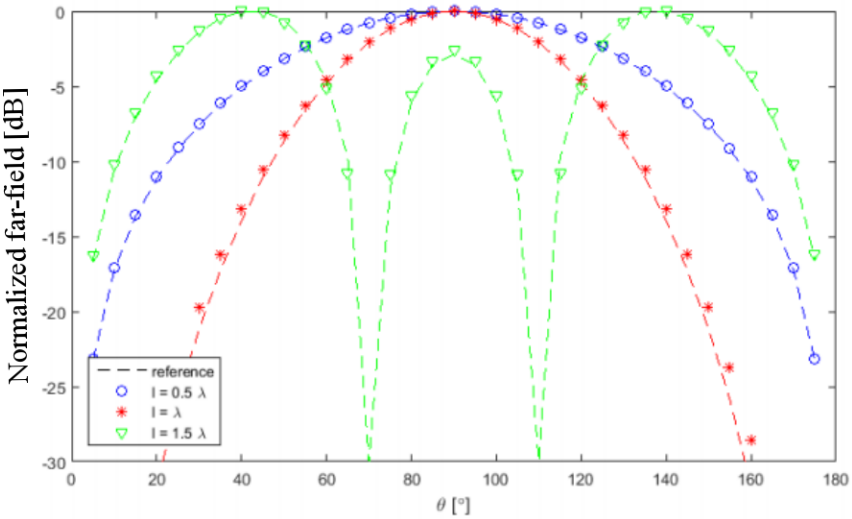

Figure 5.2: The radiated far-field pattern normalized to the maximum amplitude for the dipole constellations in Fig. 5.1.

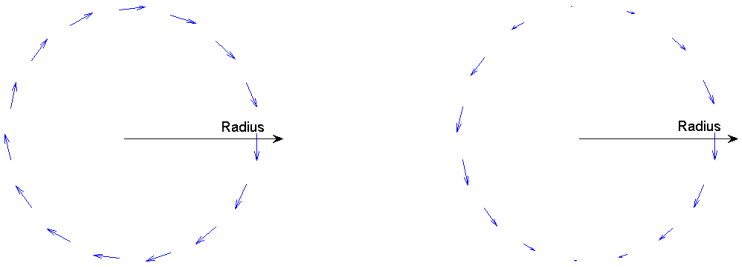

(a) Constant current distribution, $I(\phi) = I_0$.

(b) Cosinusoidal current distribution, $I(\phi) = I_0 \cos(1 \cdot \phi)$.

Figure 5.3: Examples of current distribution for the loop.

5.2 Circular loop

A loop antenna can take the form of many configurations, one of them is investigated here and it is the circular loop. Small loops, with a circumference smaller than 0.2λ is often assumed to have a constant current while loops with a circumference larger than that usually assume cosinusoidal current distributions. A constant current through the loop gives a donut shaped far-field with a maximum in the plane of the loop, $\theta = 90°$, and zero along the z-axis, $\theta = 0°$, when the radius is small compared to the wavelength. When the radius increases the field intensity in the plane of the loop diminishes and forms a null for the radius 0.61λ [7, Ch.5]. Beyond this radius the pattern attains a multilobe form. The radiation intensity for a general loop is given by (5.3) for the Bessel function J, radius a, angular frequency ω and permeability μ [7, Ch.5].

$$U = \frac{(a\omega\mu)^2|I_0|^2}{8\eta} J_1^2(ka\sin\theta) \tag{5.3}$$

A loop with a thickness of $10^{-4}\lambda$ is created with three different radii: $a = 0.1\lambda$, 0.5λ and 0.61λ. The current is assumed to be constant in ϕ-direction and zero for the ρ- and z-directions and is illustrated in Fig. 5.3a. The generated far-field patterns can be seen in Fig. 5.4. The far-field patterns agree very well with the expected behaviour. A general far-field approximation for thin circular loop antennas is given by Werner [25] and is presented in (5.4) - (5.6). The radiation intensity for the far-field is given by (2.33).

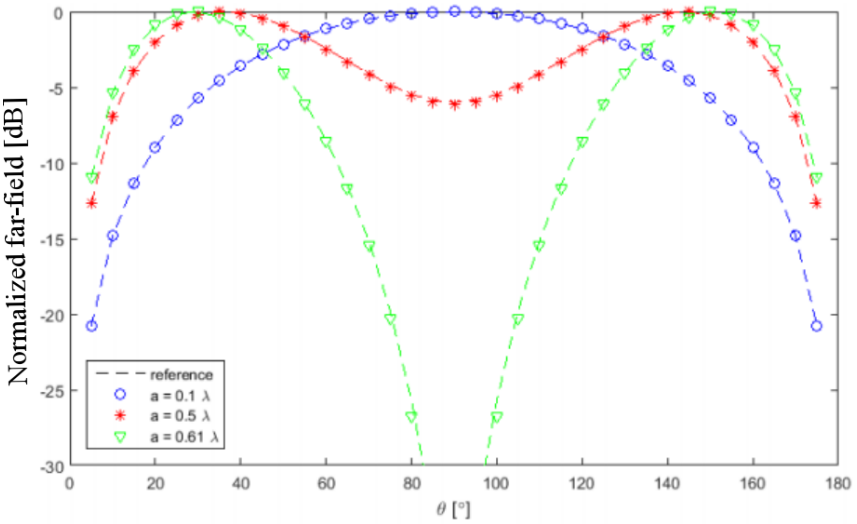

Figure 5.4: The radiated far-field pattern normalized to the maximum amplitude for a constant current in the ϕ-direction for three different radii: $a = 0.1\lambda$, 0.5λ and 0.61λ.

$$E_r \approx 0 \tag{5.4}$$

$$E_\theta \approx -\frac{\eta \cot\theta}{2}\frac{e^{-\mathrm{j}kr}}{r}\sum_{m=0}^{\infty} m(\mathrm{j})^m I_m \sin(m\phi) J_m(ka\sin\theta) \tag{5.5}$$

$$E_\phi \approx -\frac{\eta ka}{2}\frac{e^{-\mathrm{j}kr}}{r}\sum_{m=0}^{\infty} (\mathrm{j})^m I_m \cos(m\phi)\cdot\frac{1}{2}\Big(J_{m-1}(ka\sin\theta) - J_{m+1}(ka\sin\theta)\Big) \tag{5.6}$$

A loop of the same thickness as above, $10^{-4}\lambda$, is created with a radius of 0.5λ. The current was assumed to have a cosinusoidal distribution defined by $I(\phi) = I_m\cos(m\phi)$, whereas it was assumed to be zero for the ρ- and z-directions. A cosinusoidal current distribution is illustrated in Fig. 5.3b. The generated far-field patterns can be seen in Fig. 5.4. The far-field patterns agree well with the expected behaviour, but there are small deviations for the second mode low values. This is probably due to the limited accuracy of the numerically computed integrals.

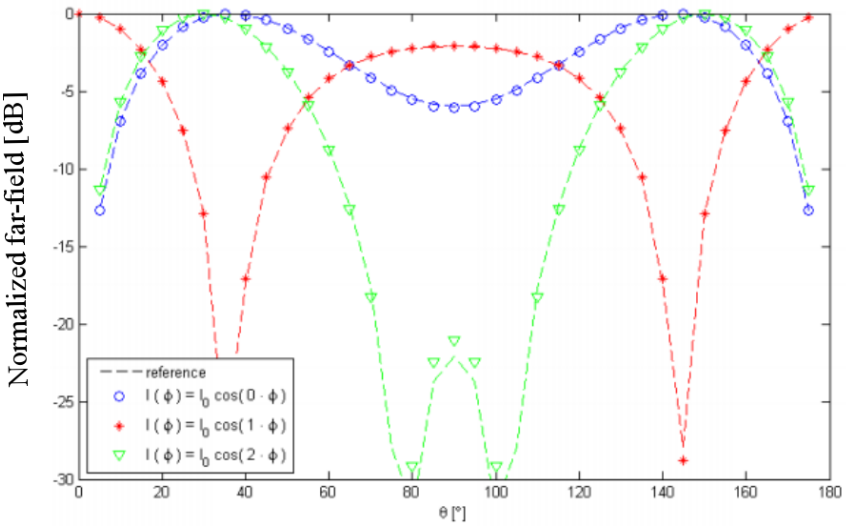

Figure 5.5: The radiated far-field pattern normalized to the maximum amplitude for a cosine distributed current in the ϕ-direction for for a radius of 0.5λ.

Chapter 6
Results

The radiation pattern and phase behaviour are analysed for a cylinder structure and disc structure, respectively. The optimization conditions are the same for all the simulations and are stated in Sec. 6.1. The cylinder structure was analysed for three different heights and two different degrees of freedom, the result is presented in Sec 6.2. Finally, a circular disc structure was analysed for three different radii in Sec. 6.3.

6.1 Optimization condition

All simulations with the MATLAB-tool were performed for the same optimization conditions for the Genetic Algorithm provided by RUAG. The convergence criterium was chosen as a maximum of 25 iterations. The number of optimizations, i.e. the number of how many times the convergence criterium was satisfied, were set to nine and number of restarts with new parameter limits were three. 20% of the old population was replaced with a new one for each generation and the parameter interval for the offsprings were 200% larger than the one for the old population. Furthermore, the population size was set to five times the chromosome size, i.e. the number of unknowns. The optimization conditions are summarized in Tab. 6.1.

6.2 Cylinder

The cylinder geometry had a radius of 3mm and was simulated for three different heights: 25m, 50mm and 100mm. The radiation frequency was set to 8.2GHz. The mask had a range from 0° to 180° with a maximum for the co-polarization between 40° and 70° and the cross-polarization mask allowed values below -15dBi. The current basis functions were chosen according to (6.1) - (6.3) where complex values for the coefficients B and D were found by optimization for each segment.

$$J_\rho = 0 \tag{6.1}$$

$$J_\phi = B_0^\phi \cdot 1 + B_1^\phi \cos(\phi') + D_1^\phi \sin(\phi') \tag{6.2}$$

$$J_z = B_0^z \cdot 1 + B_1^z \cos(\phi') \tag{6.3}$$

Table 6.1: Following optimization conditions were chosen for the genetic algorithm.

Chromosome size	Number of unknowns, (30-270)
Population size	5 · chromosome size
Convergence criterium	Maximum number of iterations, 25
Percentage of old population replaced by new	20
Percent larger parameter interval for offsprings compared to old population	200
Number of optimizations	9
Number of restarts	3

The structure of the cylinder that was used is shown in Fig. 6.1 for a height of 100mm. Two different values for the number of degrees of freedom were used for each height of the cylinder and arose because of two different choices of the number of segments.

The cost represents how far away the generated far-field is from the mask. Tab. 6.2 shows the cost for the different heights and degrees of freedom for the cylinder.

Table 6.2: Cost for cylinder structure. Note that the analysis for the height 100mm and 5 segments/ λ is performed three times, the others once.

Height [mm]	10 segments/λ	5 segments/λ	Number of unknowns
100	0.00	0.00, 0.00, 0.00	270, 140
50	2.06	2.56	140, 70
25	6.40	8.64	70, 30

In order to investigate the repeatability the same structure, with a height of 100mm, was simulated three times for the same conditions. The received cost was the same for the three simulations but the radiation patterns were slightly different, this is illustrated in Fig. 6.2.

The difference in radiation patterns for the different heights are shown in Fig 6.3 and Fig 6.4 for 10 segments/λ and 5 segments/λ, respectively.

The difference between 10 and 5 segments per wavelength for each height is illustrated in Fig. 6.5 - Fig. 6.7

Observation of the time-harmonic currents, $\mathscr{J}(\rho, \phi, z; t) = \mathrm{Re}[\boldsymbol{J}(\rho, \phi, z)e^{\mathrm{j}\omega t}]$, showed that the current direction rotated with time for all of the structures and constellations. This is illustrated for the structure of 100mm and 5 segments per wavelength in Fig. 6.8.

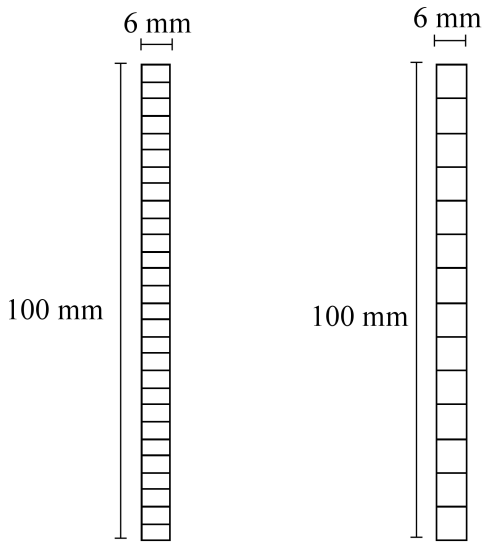

Figure 6.1: Cylinder structure separated into segments, displayed from the side with an extension in z-direction. It has a height of 100mm for 10 and 5 segments per radiating wavelength.

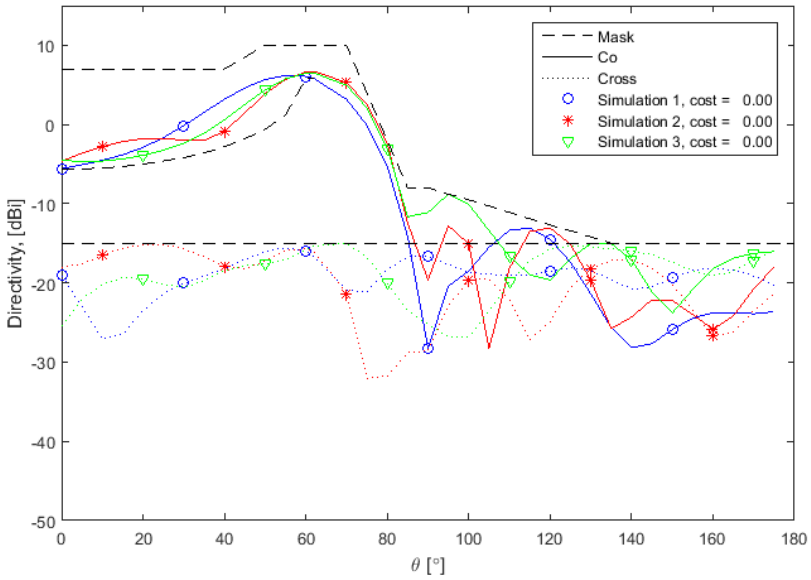

Figure 6.2: Same simulation repeated three times for the cylinder structure with height 100mm. The simulations were performed for 5 segments per radiated wavelength.

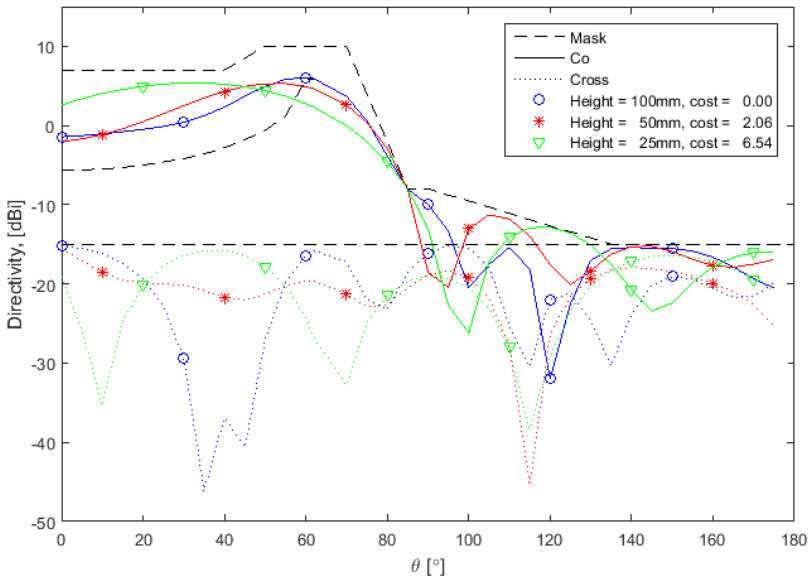

Figure 6.3: Radiation pattern for a cylinder with 10 segments/λ.

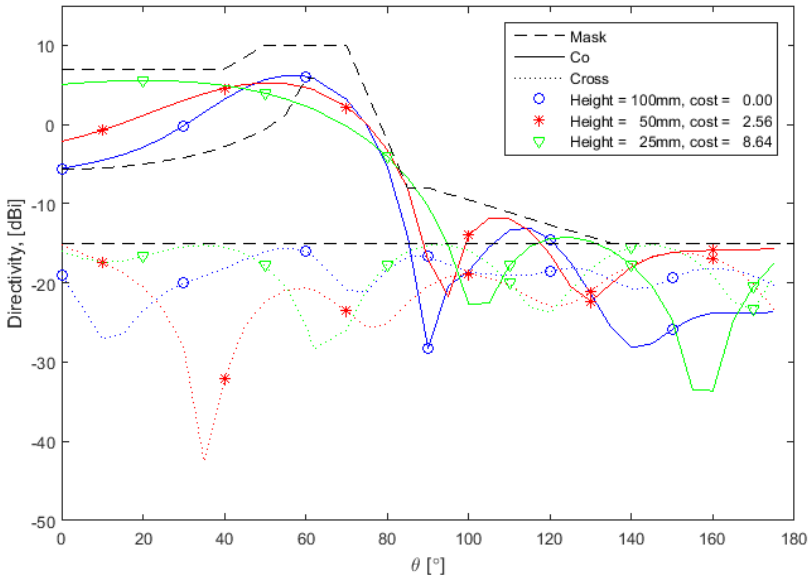

Figure 6.4: Radiation pattern for a cylinder with 5 segments/λ.

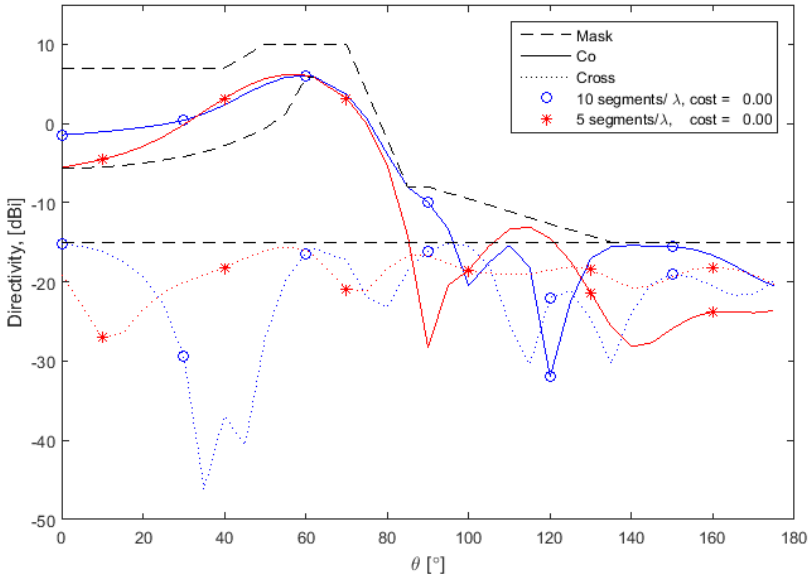

Figure 6.5: Radiation pattern for a cylinder with height 100mm.

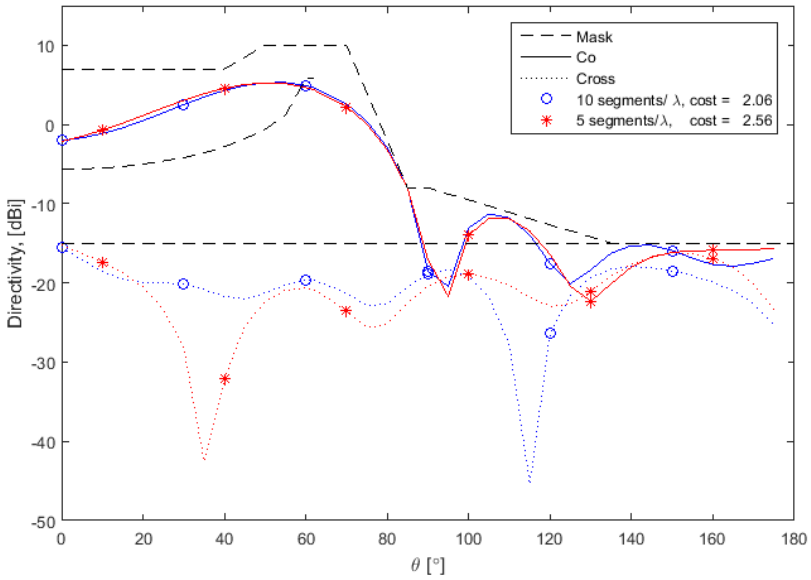

Figure 6.6: Radiation pattern for a cylinder with height 50mm.

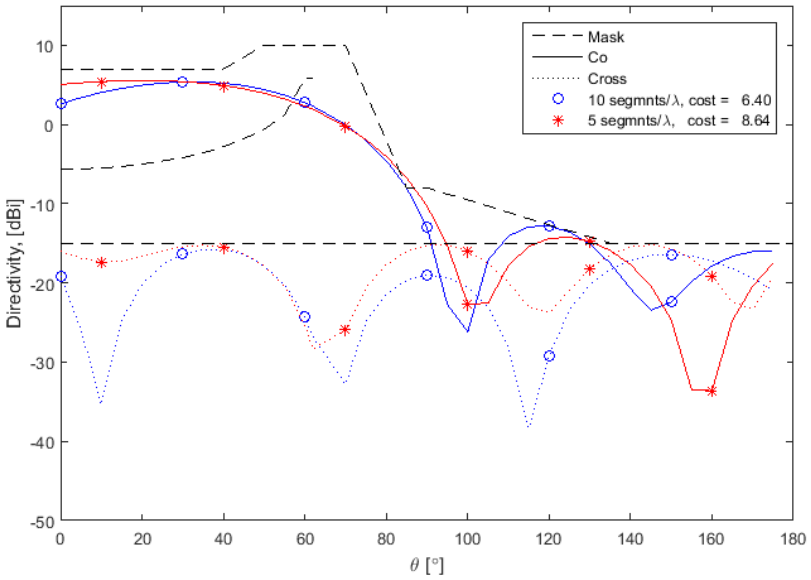

Figure 6.7: Radiation pattern for a cylinder with height 25mm.

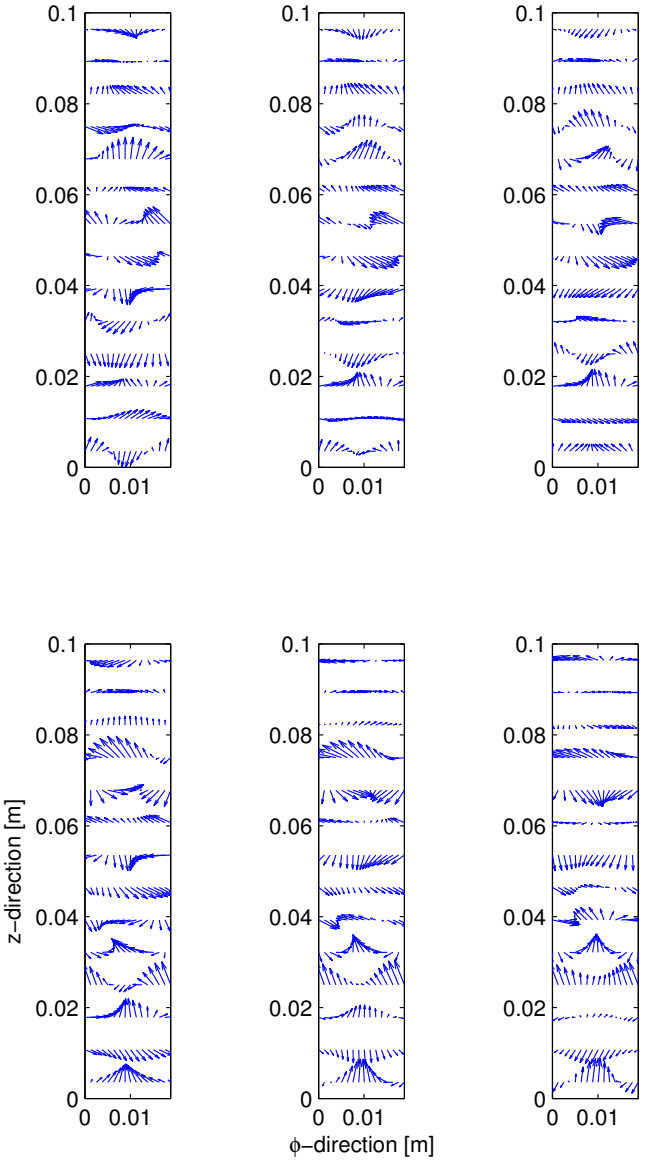

Figure 6.8: Current distribution for a cylinder with height 100mm. The phase goes between 0 and 180° with a phase step of 30°.

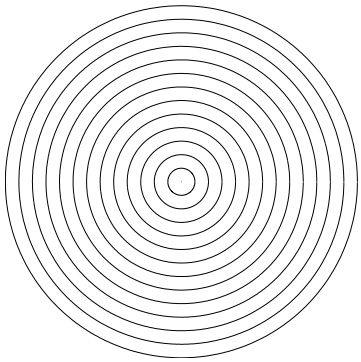

Figure 6.9: Disc structure with a radius of 200mm for 5 segments per radiating wavelength, the disc is placed in the x-y-plane.

6.3 Circular disc

The circular disc geometry lay in the x-y-plane where $z = 0$. The disc was investigated for three different radii: 200mm, 100mm and 50mm. The radiation frequency was set to 4GHz. The mask had a range from 0° to 90° with a maximum of 17dBi for the co-polarization between 0° and 8.9° and the cross-polarization mask allowed values below -15dBi. The current basis functions were chosen according to (6.4) - (6.6) where a complex value for the coefficients B and D were found by optimization for each segment.

$$J_\rho = B_0^\rho \cdot 1 + B_1^\rho \cos(\phi') + D_1^\rho \sin(\phi') \tag{6.4}$$

$$J_\phi = B_0^\phi \cdot 1 + B_1^\phi \cos(\phi') + D_1^\phi \sin(\phi') \tag{6.5}$$

$$J_z = 0 \tag{6.6}$$

The structure of the disc that was used is shown in Fig. 6.9 for a radius of 200mm.

As before the cost represents how far away the generated far-field is from the mask. Tab. 6.3 shows the cost for the different radii and the radiation pattern is shown in Fig. 6.10. The phase is illustrated in Fig. 6.11 for a phase between 0 and 180°.

Table 6.3: Cost for disc structure.

Radius [mm]	5 segments/λ	number of unknowns
200	0.00	156
100	1.82	84
50	6.00	36

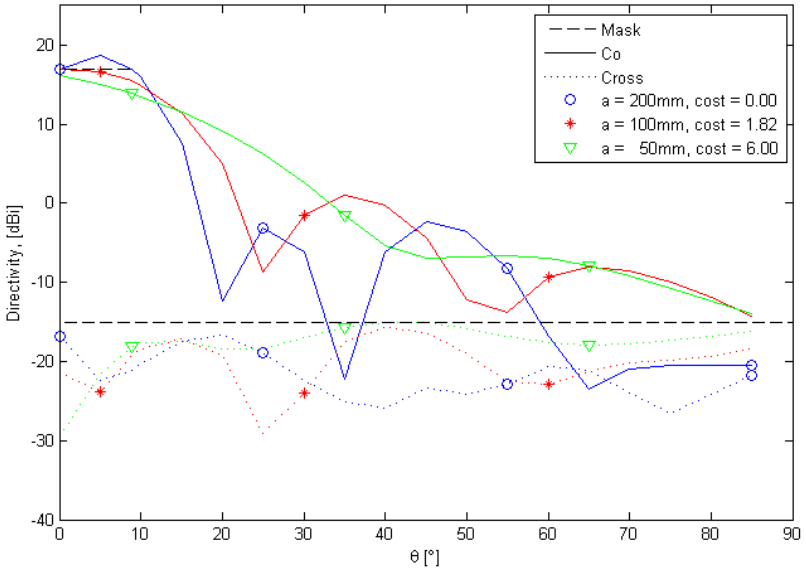

Figure 6.10: Radiation pattern for a disc with radii 50mm, 100mm and 200mm for 5 segments per wavelength. θ only goes to 90° since a ground plane is assumed.

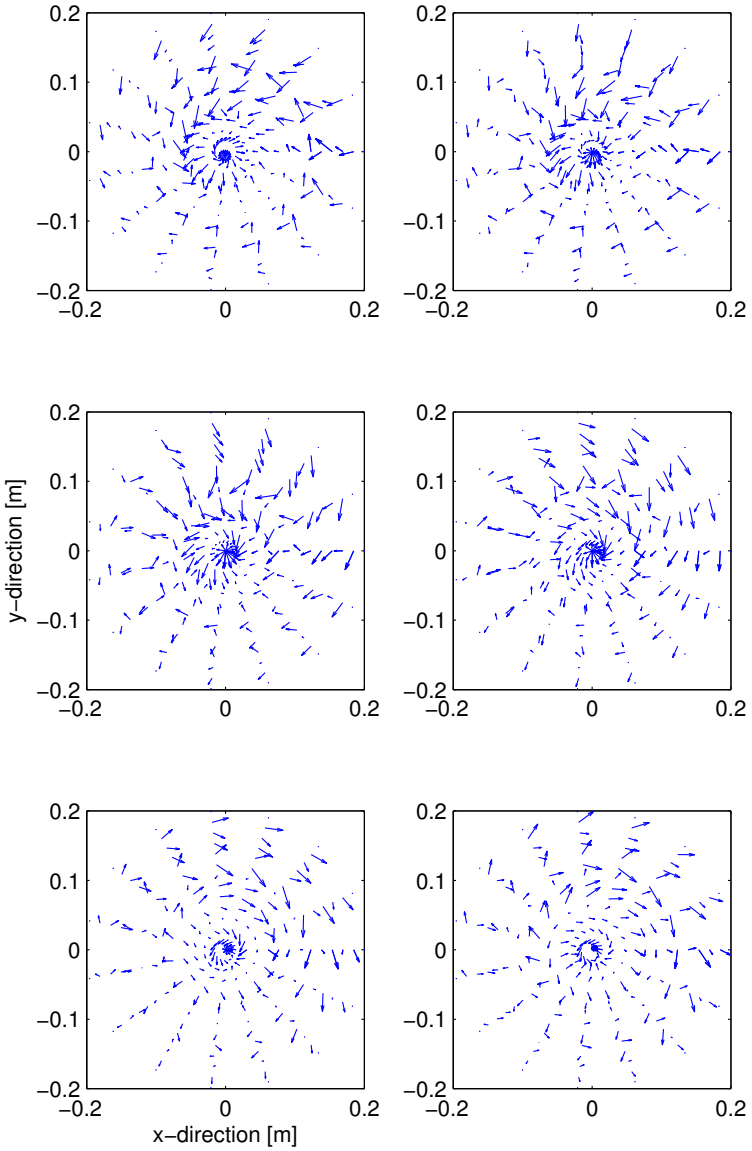

Figure 6.11: Time variation for the surface currents on the disc. The phase change between 0 and 180° with a phase step of 30°.

Chapter 7
Discussion

This chapter discusses the conditions, the code implementation and the results in order to explain results and shed light upon the strengths and weaknesses of the project. The discussion follows the order of the thesis report and starts with the optimisation method in Sec. 7.1, followed by implementation in Sec. 7.2 and verification in Sec. 7.3. The discussion around the result chapter is separated into three parts: method in Sec 7.4 including the optimization conditions and choice of current basis functions, the radiation pattern in Sec. 7.5 and the phase behaviour in Sec. 7.6.

7.1 Optimization method

The genetic algorithm was considered as a suitable optimization method for the investigation of theoretical surface currents. The main reason to this, is the combination of directed and stochastic search that explores the search space and exploits the best solution. This method minimizes the probability to find a local minimum instead of a global one. The stochastich search could also be a drawback, the practical feasible currents are not rewarded. However, in this stage of the investigation the goal has only been to find one solution of several possible.

The choice of optimization parameters depends on the optimization problem and could therefore be different for different problems. A more complex problem could require more iterations, a bigger population, more number of optimizations and more restarts. All of these elements increase the calculation time. There were two different ways of defining the convergence criterium:

- a maximum number of iterations
- a maximum parameter spread or a chosen number of iterations without improvement

For the first criterium it is possible to predict how long time the optimization will take. For the second one it is more difficult to know that, since it is not possible to affect the parameter spread or improvement of an optimization. The strength of the second criteria is that it is possible to iterate until the parameters are close to a solution, which means that the parameter spread is low and the searched value does not change that much. For the first criteria, the optimization could

be interrupt even though it is possible that a solution could be found with more iterations.

The optimization code that was used in this investigation used a predict-function. This function tries to predict a solution in order to the problem to converge faster. This failed all the time and showed warnings in MATLAB explaining that the program could not adapt a curve to the data. This could be interpreted as a discontinuity in the parameter range that is investigated.

7.2 Implementation

The way to separate the code into two different parts are time efficient. In this way no basis functions need to be calculated twice. Probably, there are more parts of the code that could be calculated in the first part in order to save time. Some parts of the program could have been written in a more time efficient way, especially the parts including the double integrals and inline-function. The inline-function is slow and combines strings and forms a function of them. For newer versions of MATLAB this function is replaced by another one which could be more time efficient. However, the time consuming inline-function and double integral does not matter that much since they are calculated in the first part of the program, that only needs to be evaluated once per structure.

7.3 Verification

The verification was performed by comparing the result with two examples. Even though the far-fields generated by the developed MATLAB-tool agreed well with the theoretical ones, a relevant question is if it is enough? A third verification was performed for cosinusoidal currents in ϕ-direction. On the other hand the third example had no radiation patterns to compare with, only formulas for the electric field. It would have been of interest to compare with a cylinder with a non-zero diameter, in order to complete the different cases for the study. Regarding the verifications that were done, the results appear to be trustworthy.

7.4 Method

The first convergence criteria that were terminated by a maximum number of iterations was chosen for the investigations in this thesis. The reason was that in this way it was possible to have control over the time for the optimization, which was not possible otherwise. However, probably the cost would have been better for the smaller structures if the convergence had been decided by the parameter spread. Sometimes it was still large when it finished.

The modes of interest for the analysis were assigned in the current basis functions. The more modes that were used, the more time consuming the calculations were. More over, more modes leads to more oscillations for the current. On the other hand the probability to find a solution is larger. In this thesis only the

zeroth and first mode are used on account of time and that more oscillations are not practically feasible.

7.5 Radiation pattern

For the same conditions several different radiation patterns within the mask could be obtained. This is illustrated in Fig. 6.2. This was expected since the problem does not have a unique solution. The optimization algorithm acts randomly and therefore different solutions are expected for restarts with the same conditions.

The tendency for a cylinder decreasing in length is the same for five and ten segments per wavelength; it is more and more difficult for the optimization algorithm to find a solution for the given criteria. This does not mean that no solution exist. Another convergence criterion or more iterations could give a zero cost for the smaller cylinders. One should keep in mind that there is a lower limit of how small the structure could be in order to generate a certain footprint, this is shown by Gustafsson et al [14] mentioned in Sec. 1.1.

Another tendency that could be noted is that the cost for the smaller cylinders is slightly higher when fewer segments are used. This behaviour is expected since there are more degrees of freedom when the structure is separated into more segments. One thing one should keep in mind is to not have too many segments. This could lead to super directivity, since the currents allows to change too fast between the segments. This needs to be investigated in greater detail.

7.6 Phase behaviour

The current vectors rotate and change direction over time. If one thinks of a helix antenna consisting of a metal wire, where the current can have only one direction, this would mean that the metal wire change its structure over the time. The same behaviour is noted for the disc. This behaviour is non-physical and not feasible for the antennas we have today. Hence, this kind of solutions should be excluded. One idea of how this could be performed is with an extra cost for rotating currents. This is presented in Ch. 8.

Chapter 8

Further Work

The surface current vectors that were found for the structures in Ch. 6 rotate as functions of time. This is classified as an unphysical behaviour, and therefore these solutions need to be rejected. This section presents an idea of how this could be performed in the cost function. The results here need to be developed further.

8.1 Time-harmonic electromagnetic fields

In many real world applications the electromagnetic waves have a cosinusoidal time variation. These electromagnetic fields are called time-harmonic and the time variation can be represented by $e^{j\omega t}$. The instantaneous current field vector $\mathscr{J}$ is represented in (8.1) and is a function of both the complex spatial current density $\boldsymbol{J}$ and the time [18, Ch.1].

$$\mathscr{J}(\rho,\phi,z;t) = \mathrm{Re}[\boldsymbol{J}(\rho,\phi,z)e^{\mathrm{j}\omega t}] \tag{8.1}$$

The equation for the instantaneous current field (8.1) can be rewritten in order to find an expression for the time independent field (8.2) - (8.5).

$$\begin{aligned}\mathscr{J}(\rho,\phi,z;t) = &\quad \Big(\mathrm{Re}(J_\rho)\mathrm{Re}(e^{\mathrm{j}\omega t}) - \mathrm{Im}(J_\rho)\mathrm{Im}(e^{\mathrm{j}\omega t})\Big)\hat{\boldsymbol{\rho}} \\ &+ \Big(\mathrm{Re}(J_\phi)\mathrm{Re}(e^{\mathrm{j}\omega t}) - \mathrm{Im}(J_\phi)\mathrm{Im}(e^{\mathrm{j}\omega t})\Big)\hat{\boldsymbol{\phi}} \\ &+ \Big(\mathrm{Re}(J_z)\mathrm{Re}(e^{\mathrm{j}\omega t}) - \mathrm{Im}(J_z)\mathrm{Im}(e^{\mathrm{j}\omega t})\Big)\hat{\boldsymbol{z}} \qquad (8.2)\\ = &\quad \Big(\mathrm{Re}(J_\rho)\cos(\omega t) - \mathrm{Im}(J_\rho)\sin(\omega t)\Big)\rho \\ &+ \Big(\mathrm{Re}(J_\phi)\cos(\omega t) - \mathrm{Im}(J_\phi)\sin(\omega t)\Big)\hat{\boldsymbol{\phi}} \\ &+ \Big(\mathrm{Re}(J_z)\cos(\omega t) - \mathrm{Im}(J_z)\sin(\omega t)\Big)\hat{\boldsymbol{z}} \qquad (8.3)\end{aligned}$$

$$
\begin{aligned}
= \quad & \mathrm{Im}(J_\rho)\left(\frac{\mathrm{Re}(J_\rho)}{\mathrm{Im}(J_\rho)}\cos(\omega t) - \sin(\omega t)\right)\hat{\boldsymbol{\rho}} \\
+ \quad & \mathrm{Im}(J_\phi)\left(\frac{\mathrm{Re}(J_\phi)}{\mathrm{Im}(J_\phi)}\cos(\omega t) - \sin(\omega t)\right)\hat{\boldsymbol{\phi}} \\
+ \quad & \mathrm{Im}(J_z)\left(\frac{\mathrm{Re}(J_z)}{\mathrm{Im}(J_z)}\cos(\omega t) - \sin(\omega t)\right)\hat{\boldsymbol{z}} \qquad (8.4) \\
= \quad & \mathrm{Im}(J_\rho)\left(\frac{\mathrm{Re}(J_\rho)}{\mathrm{Im}(J_\rho)} - \tan(\omega t)\right)\cos(\omega t)\hat{\boldsymbol{\rho}} \\
+ \quad & \mathrm{Im}(J_\phi)\left(\frac{\mathrm{Re}(J_\phi)}{\mathrm{Im}(J_\phi)} - \tan(\omega t)\right)\cos(\omega t)\hat{\boldsymbol{\phi}} \\
+ \quad & \mathrm{Im}(J_z)\left(\frac{\mathrm{Re}(J_z)}{\mathrm{Im}(J_z)} - \tan(\omega t)\right)\cos(\omega t)\hat{\boldsymbol{z}} \qquad (8.5)
\end{aligned}
$$

In order to the achieve a current streamline along one direction the instantaneous current field must be independent of ωt. This is obtained for constant ratio between the current in $\hat{\boldsymbol{\phi}}$- and $\hat{\boldsymbol{z}}$-direction for the lateral area and $\hat{\boldsymbol{\rho}}$- and $\hat{\boldsymbol{\phi}}$-direction for the base area. The conditions are defined in (8.6) and (8.7).

$$
\frac{\mathrm{Re}(J_\phi)}{\mathrm{Im}(J_\phi)} = \frac{\mathrm{Re}(J_z)}{\mathrm{Im}(J_z)} \qquad \text{lateral area} \qquad (8.6)
$$

$$
\frac{\mathrm{Re}(J_\rho)}{\mathrm{Im}(J_\rho)} = \frac{\mathrm{Re}(J_\phi)}{\mathrm{Im}(J_\phi)} \qquad \text{base area} \qquad (8.7)
$$

8.2 Idea

The radiated electric field has a time-harmonic variation represented by $e^{\mathrm{j}\omega t}$, as described in Sec. 8.1. This section stated that the instantaneous current field must satisfy (8.6) and (8.7) in order to achieve a current streamline alone one direction. For the lateral area, which is investigated in this chapter, the streamline was obtained for a constant ratio between the current in $\hat{\boldsymbol{\phi}}$- and $\hat{\boldsymbol{z}}$-direction. The condition for the lateral area from (8.6) can be rewritten as (8.8).

$$
\frac{\mathrm{Re}(J_\phi)\mathrm{Im}(J_z)}{\mathrm{Im}(J_\phi)\mathrm{Re}(J_z)} = 1 \qquad \text{lateral area} \qquad (8.8)
$$

Thus, if (8.8) is satisfied the current vector moves along a linear direction as function of the time. Due to numerical errors it is not possible to have a condition where the ratio will be exactly equal to one, there must be a small range of allowed values. As an initial test the range was chosen as (8.9).

$$
-0.5 < \mathrm{sgn}(g_1)\cdot\mathrm{sgn}(g_2)\frac{\max(|g_1|,|g_2|)}{\min(|g_1|,|g_2|)} - 1 < 0.5 \qquad (8.9)
$$

where $g_1 = \mathrm{Re}(J_\phi)\mathrm{Im}(J_z)$ and $g_2 = \mathrm{Im}(J_\phi)\mathrm{Re}(J_z)$. The reason to why the numerator always was chosen as the maximum of g_1, g_2 is that the cost then will be independent of if the numerator or the denominator is largest. The cost is zero if

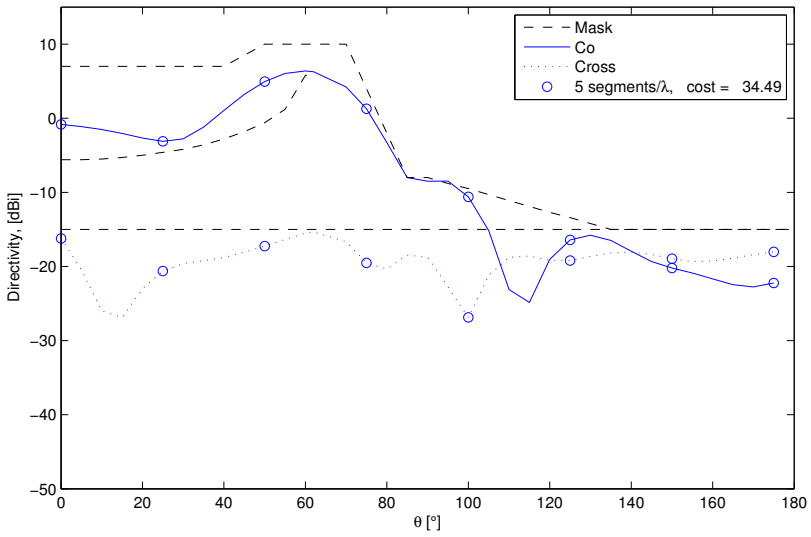

Figure 8.1: Radiation pattern for a cylinder with height 100mm and 5 segments per radiation wavelength. A cost was added for rotation current vectors.

(8.9) is satisfied, otherwise it obtained the absolute value of the ratio. The cost was summarized for all segments and angles and was added to the cost for the radiation pattern.

8.3 Results and discussion

The optimization was performed for the same conditions as before, see Ch. 6. The structure was the cylinder structure from 6.2 with a height of 100mm and five segments per radiating wavelength. The radiation pattern can be seen in Fig. 8.1. As before (Fig. 6.2) the radiation pattern satisfied the mask, on the other hand it still had a cost. This cost arose from the rotation of the current vectors. The current distribution is presented in Fig. 8.2. As before the current vectors rotated. Probably the optimization needs other conditions such as more iterations or restarts in order to the cost to reach zero (if a solution exists).

The ratio in (8.9) is graphically illustrated in Fig. 8.3. This could be seen as a measurement of "how much" it rotates. When an extra cost was added, the range for the ratio was much smaller compared to the one without. Fig 8.4 only shows the area where the condition in (8.9) is satisfied. As can be seen even the simulation without an extra cost for rotation currents had such areas. An idea could be to decrease the allowed range for the ratio if one thinks that the current vectors rotate in the shadowed areas.

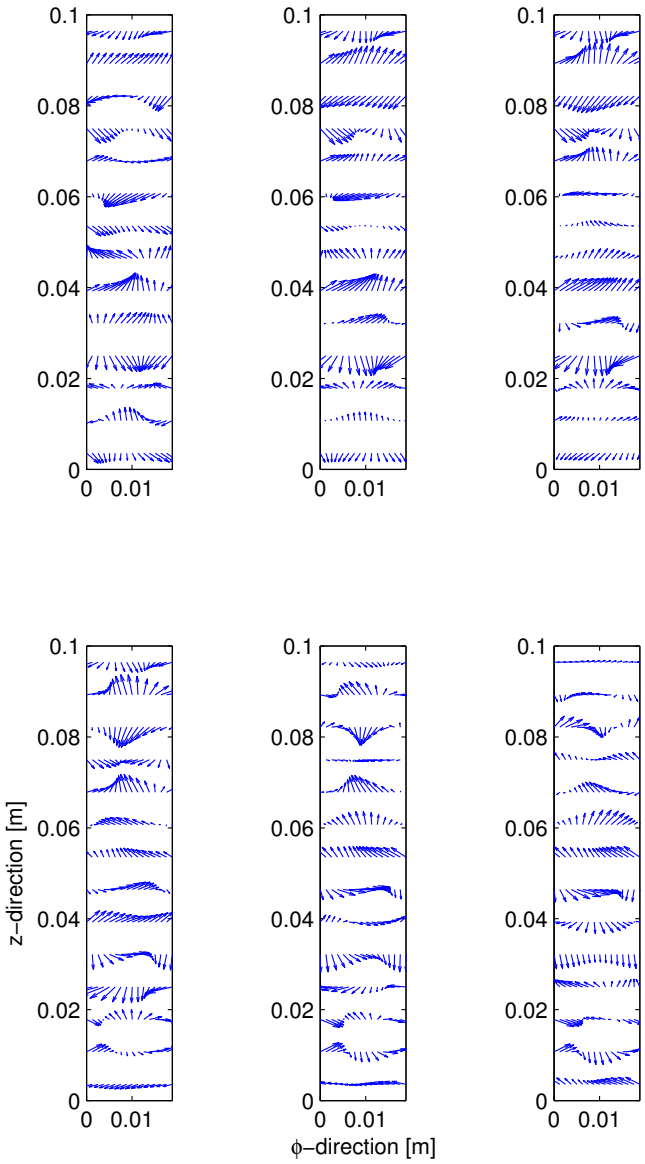

Figure 8.2: Current distribution for a cylinder with height 100mm and 5 segments per radiation wavelength. The phase goes between 0 and 180° with a phase step of 30°.

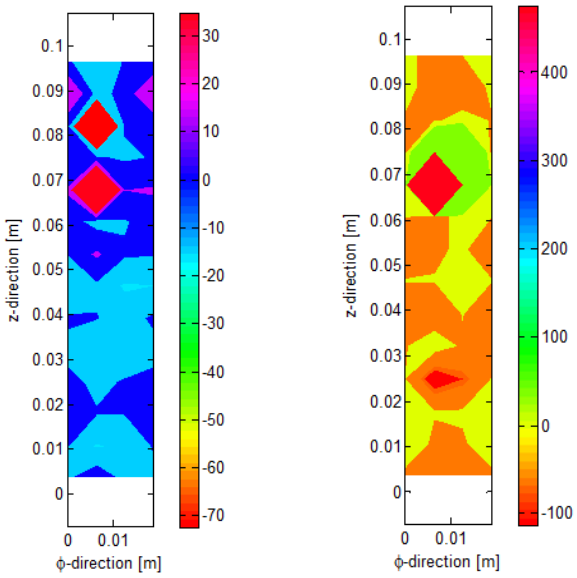

(a) Extra cost **(b)** No extra cost

Figure 8.3: Illustration of the the rotation of the current vectors. No rotation is obtaind for a value of 0.

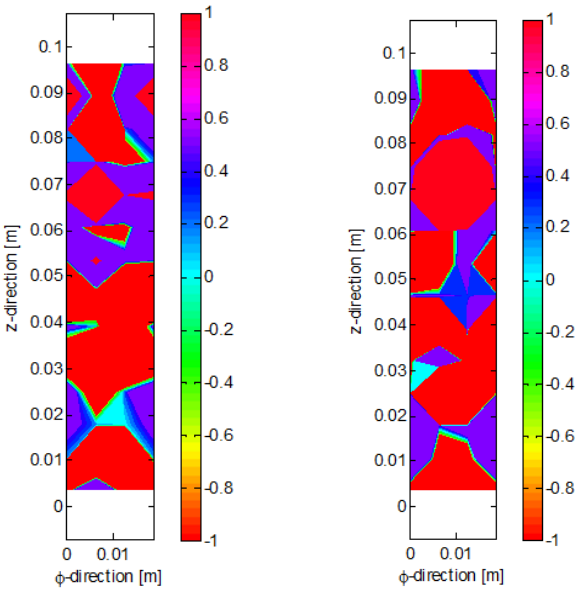

(a) Extra cost **(b)** No extra cost

Figure 8.4: The green areas represent where the condition in (8.9) is satisfied.

To conclude, it seems like an extra cost for rotation of currents could be a way forward since the spread of the values around the condition for no rotation are much smaller. The current vectors in the shadowed areas in 8.4 seem to rotate less than the other ones, like they should. However, in order to find a solution other optimization conditions are needed.

As a second step the gradient of the current vectors should be included. Limitations of how fast the current values can change over the structure will give a smoother, and possibly more practically feasible current distribution. In this way it is also possible to avoid super directivity.

Chapter 9
Conclusions

A calculation-tool has been created in MATLAB, where theoretical surface currents on a structure were calculated for a required far-field for a specified antenna outline. A genetic algorithm optimization generated feasible solutions and the MATLAB-tool evaluated the cost for it by comparing a far-field mask with the far-field given by the feasible solution.

For larger structures a solution was found for the given optimization parameters. When the structure dimensions decreased, with maintained radiation frequency, the value of the cost function rose. This does not mean that no solution exists for these structures. It should rather be seen like the analysis should be continued further for other optimization parameters in order to determine if a solution exists or not. However, it is shown that there is a lower limit for the structure size in terms of wavelength [14] that can generate a certain footprint.

This thesis started with a development of theoretical solutions. The achieved current vectors had a rotating time-behaviour, which is not physically feasible for an antenna with a fixed streamline. An idea of how to get rid of this unwanted behavior is presented as an extra contribution to the cost-function for rotating currents.

To conclude, a MATLAB-tool was created and it found theoretical solutions for a specified antenna structure and a required far-field. However, further work needs to be performed regarding practical solutions.

References

[1] M. Levin and M. Miller, "Maxwell a treatise on electricity and magnetism," *Uspekhi Fizicheskikh Nauk*, vol. 135, no. 3, pp. 425–440, 1981.

[2] C. Balanis *et al.*, "Antenna theory: A review," *Proceedings of the IEEE*, vol. 80, no. 1, pp. 7–23, 1992.

[3] J. D. Kraus, "Antennas," 1988.

[4] S. Silver, *Microwave antenna theory and design*. Iet, 1949, no. 19.

[5] G. T. Di Francia, "Super-gain antennas and optical resolving power," *Il Nuovo Cimento (1943-1954)*, vol. 9, pp. 426–438, 1952.

[6] B. Elbert, *Introduction to satellite communication*. Artech house, 2008.

[7] C. A. Balanis, *Antenna theory: analysis and design*. Harper and Row, 1982, vol. I.

[8] S. A. Schelkunoff, "A mathematical theory of linear arrays," *Bell System Technical Journal*, vol. 22, no. 1, pp. 80–107, 1943.

[9] H. G. Booker and P. Clemmow, "The concept of an angular spectrum of plane waves, and its relation to that of polar diagram and aperture distribution," *Proceedings of the IEE-Part III: Radio and Communication Engineering*, vol. 97, no. 45, pp. 11–17, 1950.

[10] P. Woodward, "A method of calculating the field over a plane aperture required to produce a given polar diagram," *Journal of the Institution of Electrical Engineers-Part IIIA: Radiolocation*, vol. 93, no. 10, pp. 1554–1558, 1946.

[11] P. Woodward and J. Lawson, "The theoretical precision with which an arbitrary radiation-pattern may be obtained from a source of finite size," *Journal of the Institution of Electrical Engineers-Part III: Radio and Communication Engineering*, vol. 95, no. 37, pp. 363–370, 1948.

[12] L. Ricardi, "Radiation properties of the binomial array," *Microwave J*, vol. 15, no. 12, pp. 20–21, 1972.

[13] C. Dolph, "A current distribution for broadside arrays which optimizes the relationship between beam width and side-lobe level," *Proceedings of the IRE*, vol. 34, no. 6, pp. 335–348, 1946.

[14] M. Gustafsson, M. Cismasu, and B. L. G. Jonsson, "Physical bounds and optimal currents on antennas," *Antennas and Propagation, IEEE Transactions on*, vol. 60, no. 6, pp. 2672–2681, 2012.

[15] M. Gustafsson and S. Nordebo, "Optimal antenna currents for q, superdirectivity, and radiation patterns using convex optimization," *Antennas and Propagation, IEEE Transactions on*, vol. 61, no. 3, pp. 1109–1118, 2013.

[16] M. Gen, R. Cheng, and L. Lin, *Network models and optimization: Multiobjective genetic algorithm approach*. Springer Science & Business Media, 2008.

[17] W. C. Gibson, *The method of moments in electromagnetics*. CRC press, 2014.

[18] C. A. Balanis, *Advanced engineering electromagnetics*. John Wiley & Sons, 1989, vol. I.

[19] A. S. Committee *et al.*, *IEEE Standard Definitions of Terms for Antennas*. IEEE, 1993.

[20] C. A. Balanis, *Modern antenna handbook*. John Wiley & Sons, 2008.

[21] P.-S. Kildal, *Foundations of antennas: a unified approach*. Studentlitteratur, 2000.

[22] U. Diwekar, *Introduction to applied optimization*. Springer Science & Business Media, 2008, vol. 22.

[23] R. K. Arora, *Optimization: Algorithms and Applications*. CRC Press, 2015.

[24] M. Matlab, *Natick, MA: Mathworks*. Inc, 1999.

[25] D. H. Werner, "An exact integration procedure for vector potentials of thin circular loop antennas," *Antennas and Propagation, IEEE Transactions on*, vol. 44, no. 2, pp. 157–165, 1996.

LUND
UNIVERSITY

Series of Master`s theses
Department of Electrical and Information Technology
LU/LTH-EIT 2016-495

http://www.eit.lth.se